THESIS FOR THE DEGREE OF DOCTOR OF PHILOSOPHY

Modeling colloidal nanoparticles: From growth to deposition

Joakim Löfgren

Department of Physics
CHALMERS UNIVERSITY OF TECHNOLOGY
Göteborg, Sweden 2019

Modeling colloidal nanoparticles:
From growth to deposition
Joakim Löfgren

ISBN 978-91-7905-176-1

Doktorsavhandlingar vid Chalmers tekniska högskola
Ny serie nr 4643
ISSN 0346-718X

Department of Physics
Chalmers University of Technology
SE-412 96 Göteborg, Sweden
Telephone +46317723252

Cover: The *Blasphemous Monstrosity*, a small, thiolated gold nanoparticle [1].
Chalmers reproservice
Göteborg, Sweden 2019

Modeling colloidal nanoparticles: From growth to deposition

Joakim Löfgren
Department of Physics
Chalmers University of Technology

Abstract

In recent decades metal nanoparticles (NPs) have been the subject of intense research. The interest stems from the NPs physicochemical properties that can be conveniently tuned through, e.g., their size, shape or composition. A good example is the selective absorption of electromagnetic radiation exhibited by gold nanorods, which is leveraged for applications in sensing and medicine. In order to realize the full potential of technologies reliant on NPs and ensure fitness for commercial use, facile fabrication methods that allow for a high degree of shape and size control are required. For this purpose, wet-chemistry-based synthesis in which colloidal NPs self-assemble into a targeted morphology have emerged as promising candidates. Development and refinement of synthesis protocols is, however, hampered by a lack of theoretical understanding of the complex chemical environment in NP solutions. As a result, experimental workers are often left to rely on intuition. This applies not only to the growth process itself, but also later down the processing chain, e.g., during NP deposition.

This thesis aims to address two problem areas relating to NP growth and deposition where current models need improvement. The first such area concerns the description of ionic and molecular adsorption on the surface of metal NPs. We show how combining thermodynamic modeling, density functional theory and experimental data can lead to more realistic NP shape predictions. A closely related subject is the growth mechanism of anisotropic gold nanorods, which has been a subject of debate for almost the three decades. Here, we consider possible avenues through which shape anisotropy can arise using insight from molecular dynamics simulations. The second problem area is the description of forces between NPs and nearby surfaces, which is relevant, e.g, for applications reliant on NP deposition. A model based on Derjaguin-Landau-Verwey-Overbeek theory is developed that describes how the shape and composition of a surface affects particle deposition.

Keywords: colloidal nanoparticles, gold, anisotropic, nanorods, modeling, density functional theory, thermodynamics, dispersive interactions, van der Waals, deposition, DLVO

LIST OF APPENDED PAPERS

This thesis is based on work presented in the following papers:

I **Understanding the Phase Diagram of Self-Assembled Monolayers of Alkanethiolates on Gold**
Joakim Löfgren, Henrik Grönbeck, Kasper Moth-Poulsen, and Paul Erhart
The Journal of Physical Chemistry. C, 120, 12059 (2016)

II **Quantitative assessment of the efficacy of halides as shape-directing agents in nanoparticle growth**
Joakim Löfgren, Magnus Rahm, Joakim Brorsson, and Paul Erhart
In preparation

III **Modeling the growth of gold nanorods**
Narjes Khosravian, Joakim Löfgren and Paul Erhart
In preparation

IV **Understanding Interactions Driving the Directed Assembly of Colloidal Nanoparticles**
Johnas Eklöf-Österberg, Joakim Löfgren, Paul Erhart, Kasper Moth-Poulsen
Submitted for publication

V **libvdwxc: a library for exchange correlation functionals in the vdW-DF family**
Ask Hjorth Larsen, Mikael Kuisma, Joakim Löfgren, Yann Pouillon, Paul Erhart, and Per Hyldgaard
Modelling and Simulation in Materials Science and Engineering, 25, 065004 (2017)

PUBLICATIONS NOT INCLUDED IN THIS THESIS

The following publications are outside the scope of this thesis:

Electric field-controlled reversible order-disorder switching of a metal surface
Ludvig de Knoop, Mikael Juhani Kuisma, Joakim Löfgren, Kristof Lodewijks, Mattias Thuvander, Paul Erhart, Alexander Dmitriev and Eva Olsson
Physical Review Materials 2, 085006 (2018)

The author's contribution to the papers:

I The author carried out the calculations, analysis and wrote most of the paper.

II The author carried out the calculations, analysis and wrote most the paper.

III The author wrote the code, carried out the calculations, theoretical analysis and wrote part of the paper.

IV The author participated in the analysis of the calculations and wrote part of the paper.

V The author contributed to the benchmarking calculations, testing of the software and writing of the paper.

Contents

List of Abbreviations

AR aspect ratio 9, 14

CMC critical micelle concentration 9

CTAB cetyl trimethyl ammonium bromide 9–11

DFT density functional theory vii, 18–20

DLVO Derjaguin-Landau-Verwey-Overbeek 23, 24, 27

EDL electrostatic double layer 23, 27

LPBE linearized Poisson-Boltzmann equation 26

LSPR localized surface plasmon resonance 11, 12

NP nanoparticle 1–7, 11–13, 15, 16, 18, 23, 28

PB Poisson-Boltzmann 26, 27

SEI surface element integration 27, 28

vdW van-der-Waals 23, 24, 27, 28

ZPE zero-point energy 19

1 Introduction

Nanoscience is defined as the study and development of systems having one or more dimensions lying in the range of 1 to 100 nm. At this length scale quantum mechanical effects can lead to new or altered properties of a material that do not manifest on macroscopic scales.

Historically, the use of nanoscale systems long predates any theory or systematic attempt at understanding the underlying phenomena, as evidenced, e.g., in the stained glass of church windows, resulting from the interaction of light with nanoparticles present in the glass [2]. Only with the advent of modern physics during the 20th century has theoretical understanding, manufacturing and precise manipulation of such systems become possible. Today, nanoscience constitutes an enormous research field with applications ranging from consumer grade products to next generation technologies in electronics [3–6], medicine [7–9] and renewable energy systems [10–12].

1.1 Metal nanoparticles

Metal nanoparticles (NPs) represent a prominent family of nanosystems, consisting of solid particles of various shapes where all dimensions are in the nanometer range. In applications, NPs can assume a multitude of roles, e.g., functioning as building blocks, delivery agents, catalysts, sensing devices or therapeutic agents. Below, we elaborate on these uses and discuss how they relate to different NP properties. Extra emphasis is put on the effect of physical properties such as shape, size, composition, that can conveniently be tuned during fabrication. Indeed, the versatility offered by such "handles" is one of the primary driving forces behind the extensive research into NPs.

For the use of NPs as building blocks or delivery agents, the reactivity of its surface, or more precisely the propensity of atoms and molecules to adsorb on the surface is one

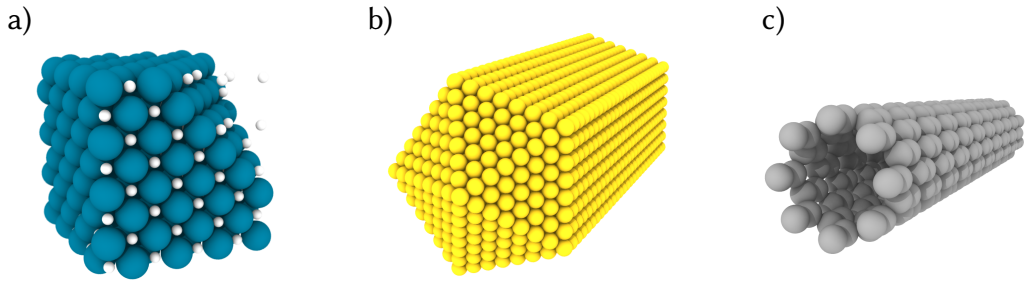

Figure 1.1: Various nanomaterials and their applications. a) Hydrogen sorption in Pd enables the development of hydrogen sensing devices. b) The tunable optical properties of Au nanorods can be used for cancer treatment. c) Carbon nanotubes have excellent mechanical properties that can enhance the strength of materials.

of the most important considerations. Adsorbed molecules can act as linkers between nanoparticles to build circuits [13, 14] or as carriers that pharmaceuticals can "piggy-back" onto and create drug delivery systems [15–17]. While the origin of metal surface reactivity can be surprisingly subtle in many cases [18], computational methods can nowadays aid us in understanding and predicting its dependence on parameters such as NP shape and composition.

An oft-mentioned fact about NPs is the high surface-to-volume ratio found in a sample of NPs compared to an otherwise equivalent bulk sample. The usefulness of having a large amount of surface area is easy to appreciate if we consider heterogenous catalysis, where the use of NPs has been actively studied since the middle of the 20th century [19]. Here, transient binding of reactants to catalytically active sites on the NP surface gives rise to new reaction pathways that can lower the reaction energy barrier. NP-based catalysts thus have the potential to greatly expedite reactions due to the large amounts of surface area exposed.

Another large group of applications are enabled by the scattering, adsorption or emitting of electromagnetic radiation by NPs. Within the context of this thesis, a highly relevant example is provided by gold nanorods (Fig. 1.1b). Like silver [20], gold NPs exhibit strong localized surface plasmon resonances (LSPRs) that allow them to efficiently absorb incoming light in certain frequency windows [21]. In the case of nanorods, the shape anisotropy leads to a splitting of the LSPR into one longitudinal and one transversal mode. The frequency of the longitudinal resonance mode is tunable through the

aspect ratio of the rod, providing control over the optical response of the rod. This is the basis of photothermal cancer therapy where nanorods are targeted at a tumor and subsequently irradiated at the LSPR frequency. The adsorbed light is then given off as heat to the environment, resulting in the destruction of the cancer cells [22, 23]. In a similar vein, Pd NP have been investigated as a means for building hydrogen sensors. The construction of such sensors is crucial for the use of hydrogen as a renewable energy source since fuel leakage can easily lead to volatile mixtures of hydrogen and air. The key idea is that hydrogen can be stored in the interstitial sites of Pd (Fig. 1.1b). The amount of hydrogen stored depends on the partial pressure of hydrogen in the surrounding gas-phase, and any changes resulting from a sudden release of hydrogen can be detected as shift in the peak of the NPs LSPR spectrum [24].

1.2 Challenges for nanotechnology

Despite the potential of NP-based technologies, many of the applications are still in their infancy. There is thus no shortage of challenges that have to be addressed before they can be adopted for widespread use. One challenge concerns up-scaling; industrial production requires cost-effective manufacturing processes while historically NPs have been created in specialized laboratories using time-consuming methods and expensive materials. In the recent decades, top-down methods have emerged as a scalable route to obtaining nanomaterials for use in, e.g., electronics. They are, however, less suited for NPs since they often rely on surface modification via lithography. On the other hand, bottom-up, wet chemical synthesis offers a simple way of obtaining NPs where properties of the products such as size, shape and composition are tunable through various synthesis parameters and components. A key issue here, however, is the lack of theoretical understanding concerning the synthesis processes themselves. Consequently improvements to protocols are mainly due to heuristics and ad hoc experimentation rather than the result of a rational design process, an approach that is ultimately limited.

From a societal perspective, there are also safety issues regarding nanotechnology as a whole, including toxicity, environmental pollution and the development of nanomaterial-based weaponry. For instance, the interactions of NPs with complex biological environments such as the inside of a human body are in general not well understood. The small size of the particles facilitates transport through the body and provides a large available surface for interactions with surrounding biomolecules. Indeed, studies have concluded that NPs entering the human body through the airways [25] or gastrointestinal tract [26] can be taken up in the blood circulation and distributed to various organs via the liver and the spleen. The clearance rate of NPs from the body depends on the specific particle properties and may proceed via different mechanisms [27]. Long term retention of NPs leads to concerns regarding, e.g., cell damage as the result of

excess generation of reactive oxygen species due to the presence of the particles [28]. There is thus a need for detailed experimental as well as theoretical studies with regards to the interactions in the interfacial region between NP surface and organic molecules.

1.3 Thesis aim and outline

The overarching goal of this thesis is to help bridge the gap between theoretical modeling and application for a number of topics related to the challenges described in Sect. 1.2. Most prominently featured are issues related to adsorption of molecules and ions at metal surfaces, where the importance of properly accounting for dispersive interactions and solvation effects is investigated in **Papers I** and **II**. From a more technical perspective, the incorporation of dispersive interactions into density functional theory (DFT), which is extensively used throughout the first two papers, is described in **Paper V**. While the ability to model NP surfaces from first-principles methods such as DFT is extremely useful in modeling the growth of NPs, the length and time scales involved often necessitate the use of other methods, e.g., molecular dynamics (MD) in order to gain a more complete understanding. This is the case for gold nanorod growth, where the origin of their anisotropy and the growth mechanism has been under debate for almost two decades. Here, **Paper III** presents a critical review of recent modeling efforts, primarily based on MD. Finally, in **Paper IV**, another step upwards in the length and time scales is taken as the modeling of NP deposition is addressed using Derjaguin-Landau-Verwey-Overbeek (DLVO) theory.

A background on colloidal NPs including a brief historical perspective, fabrication methods, stability, and optical properties is provided in Chapter 2. In particular, a general overview of wet-chemical synthesis of NPs via seed-mediated growth is provided and subsequently exemplified by the synthesis of gold nanorods. Chapter 3 begins with an overview of various aspects of colloidal modeling and relevant methodology. The next two sections provide background for the two principal modeling aspects most relevant for the thesis. The first such aspect is the thermodynamics of surfaces and NP shape prediction, where a detailed account is also provided for how to combine the derived expression with DFT. The second aspect concerns interparticle and surface forces, focusing on DLVO theory. Since DFT calculations play a central role in this thesis, the underlying theory is presented separately in Chapter 4. Here, an important topic is that of dispersion-corrections, which play a prominent role in several of the appended papers, which are summarized in Chapter 5.

2 Colloidal nanoparticles

Elements combine and change into compounds. But that's all of life, right? It's the constant, it's the cycle. It's solution, dissolution. Just over and over and over. It is growth, then decay, then transformation.

Walter White

2.1 Historical highlights

The scientific study of colloidal NPs began in the 1850s with Michael Faraday, who was interested in the optical properties of thin gold sheets [29]. As a by-product of this research he obtained a gold sol and began a systematic investigation of colloidal gold created from the reduction of a solution of gold chloride by phosphorus. He deduced, among other things, that the characteristic red tint of the sol was due to the interaction of light with suspended gold particles invisible to the naked eye [29]. Colloid science as a whole, however, did not start to pick up momentum until the end of the 19th century. In particular regarding NPs there are several highlights from this period. The first synthesis of colloidal silver from reduction of silver citrate by iron(II) citrate was carried out in 1889 by Lea [30]. Building on the work of Faraday, Zsigmondy invented the nucleus method in 1905 for the synthesis of gold sols [31]. Chloroauric acid ($HAuCl_4$) was reduced by white phosphorus creating a solution of NPs seeds 1–3 nm in diameter. To obtain larger NPs a growth solution was prepared in a vial and initially kept separate from the seeds. This growth solution contained more gold salt, which was reduced with formaldehyde. Addition of the seeds to this growth solution resulted in the formation of gold NPs 8 to 9 nm in diameter. Conceptually, Zsigmondy's method is a predecessor

to much of modern colloidal NP synthesis that follow the same logic of letting seed particles grow into a target morphology.

Significant advancements were also made on the theoretical side. The rapid motion undergone by suspended colloidal particles and their stability against gravity was explained in terms of Brownian motion by Einstein [32] and Smoluchowski [33]. The optical properties of metal sols were elucidated by Mie [34] and Gans [35], who derived shape-dependent expressions for the scattering and absorption of incident light by the particles from Maxwell's equations, providing an explanation for the observations made by Faraday some fifty years earlier.

2.2 Fabrication methods

Fabrication of nanomaterials is often categorized as being either top-down or bottom-up. A top-down method starts from a bulk sample and then successively removes material until the desired shape or form is obtained as done in, for instance, optical or electron lithography. Conversely, bottom-up fabrication is the assembly of a nanomaterial from smaller constituent pieces. Both categories of nanofabrication have their distinct advantages and limitations, but only bottom-up, wet-chemistry approaches will be dealt with here since they provide the most facile route to obtaining NPs while top-down methods are more suitable for, e.g., surface patterning [36].

There are two principal approaches to bottom-up fabrication: gas-phase and wet-chemical (liquid-phase) synthesis. A gas-phase method starts from a precursor which is evaporated, forming an intermediate state containing monomers[1]. Nucleation in this intermediate state then leads to primary particles that form NPs, e.g., by coalescing [37]. The resulting colloid of solid particles suspended in a gas is known as an *aerosol*. Liquid-phase synthesis processes follow a similar pattern. A precursor is created, for instance by dissolution of a solid, and an intermediate state of monomers is produced from chemical reactions. Nucleation in the monomer solution then leads to primary particles that subsequently form NPs through e.g., diffusive growth [38]. Generally, gas-phase routes yield very pure product particles with minimal by-products, and scale better than their liquid-phase relatives. When it comes to the fabrication of anisotropic shapes, however, wet-chemical synthesis is the superior approach.

One example of a wet-chemical synthesis protocol has already been encountered, namely Zsigmondy's nuclear method described in the previous section. Another relevant example is the Turkevich method [39], which is one of the most commonly employed protocols for the synthesis of spherical gold NPs[2]. A solution of chloroauric acid is heated to its boiling point and then a solution of sodium citrate ($Na_3C_6H_5O_7$) is added. The sodium citrate will act both to reduce the gold and as a capping agent for

[1] In this text, a monomer refers to a unit of the precursor compound that supplies the growth.

[2] It can also be used to obtain silver NPs.

the subsequently formed NPs, electrostatically stabilizing them against agglomeration by forming a negatively charged surface layer.

2.2.1 Seeded growth

Shape-controlled wet-chemical synthesis of metal NPs is perhaps most easily achieved based on the concept of seeded, or seed-mediated, growth. Much like in Zsigmondy's nucleus method, the key characteristic of seeded growth is the preparation of a NP seed solution, which is later added to a separately prepared growth solution in order to achieve the desired product. The decoupling of the nucleation and growth stages allows for better control over size and shape of the final particles, at the cost of a more laborious synthesis process compared to one-pot protocols. Modern seeded growth began with the synthesis of gold nanorods in 2001 by Murphy and coworkers [40], who also demonstrated that it could be used to achieve greater size control when synthesizing spherical gold NPs [41]. Following the same general principles, seed-mediated growth protocols have since been reported for a variety of other metals such as Ag, Pd, Pt, and Cu [42–44]. In a typical seeded growth protocol the seed solution will consist of a metal salt, a reducing agent and a capping (stabilizing) agent (Fig. 2.1) to prevent aggregation of the seeds and possibly alter the surface energetics to expose certain facets. The growth solution has the same basic ingredients but different compounds may be used depending on the goal of the synthesis. For instance, another type of metal salt may be used if bimetallic structures are targeted [45]. Furthermore, the growth solution reducing agent must be sufficiently weak to prevent nucleation of additional seeds. This allows for metal ions to be reduced in a catalytic reaction near the surface of the seeds [40]. The resulting growth of the pre-existing seeds can then be guided towards anisotropic shapes by adding a second capping agent. In practice, the basic synthesis recipe described here is often augmented with additives or co-surfactants in order to improve yield, monodispersity or to achieve different shapes. In terms of the growth stage, one can distinguish between one-step and multi-step protocols [46]. The latter are characterized by several iterated growth cycles, during which more growth solution is added to aliquots drawn from the current seed/growth solution mix.

Deciphering the precise role played by the various ingredients is very difficult as they may vary on a method-to-method basis and synergistic effects can make the individual impact of a compound hard to disentangle from the whole. The descriptions provided above, while intuitive, are too simplistic to adequately account for the myriad permutations of seeded growth protocols.

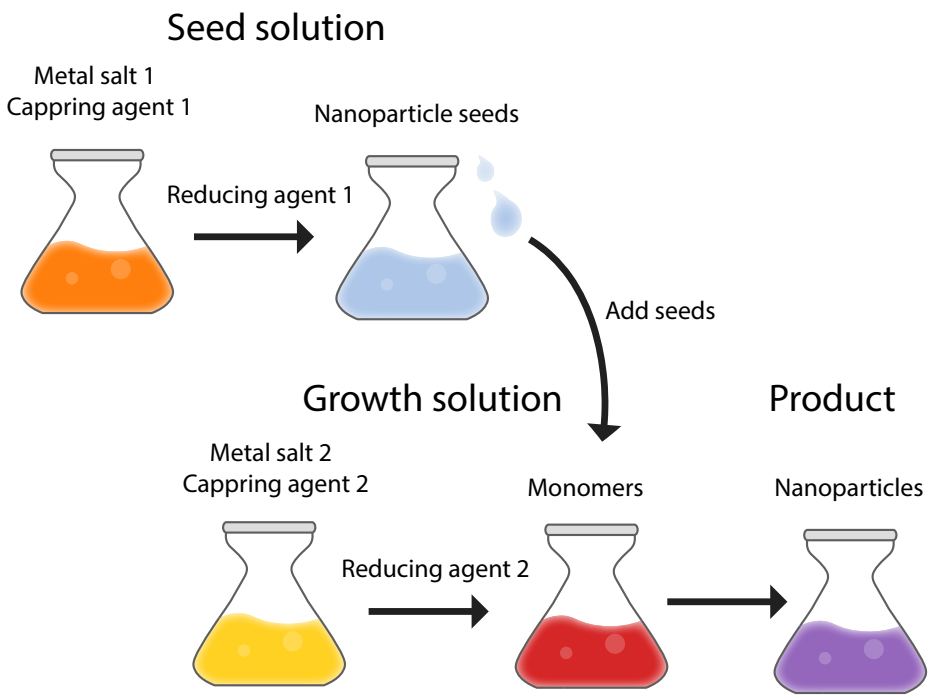

Figure 2.1: A general outline for seed-mediated growth protocols. Decoupling the nucleation and growth stages by separately synthesizing seeds and then adding them to a growth solution of monomers allows for more precise shape and size control. Depending on the desired outcome, metal salt and capping agents can vary between the two solutions. The growth solution reducing agent is constrained by the requirement that no additional nucleation take place.

2.3 Gold nanorods

Gold nanorods are the most extensively studied synthesis products of seed-mediated growth owing to their physicochemical properties, spurring research into a multitude of potential applications in, e.g., drug delivery, cancer therapy and sensing. Furthermore, they also pose a very interesting problem from a theoretical perspective with many questions that remain unanswered regarding, e.g., the origin of the symmetry breaking event that occurs in the evolution from spherical seeds to nanorods. As the first seeded growth method to gain widespread popularity it is also particularly appropriate as a concrete illustration of the generalized description presented in Sect. 2.2.1.

2.3.1 Synthesis

Turning to the actual nanorod synthesis procedure, it should be noted that since its advent many variations of the original protocol have spawned that try to improve, e.g., yield or control over the AR. The latter is especially important since it allows for tuning the plasmonic response (Sect. 2.4). Rather than providing an exhaustive list of all possibilities, focus will be on the original three-step protocol by Murphy [40] and the nowadays more commonly employed silver-assisted one-step protocol [47].

Three-step protocol (P-1). This protocol follows the general seeded growth procedure outlined in Fig. 2.1. The seeds are prepared by reducing $HAuCl_4$with ice-cold sodium borohydride[3] ($NaBH_4$) and adding (trisodium) citrate to stabilize the seeds against aggregation. In the growth solution the reduction of $HAuCl_4$is instead accomplished with ascorbic acid (AA) in the presence of CTAB surfactant (Fig. 2.2). A concentration of around 0.1 M CTAB is required in order to obtain nanorods, which is 100 times more than the first CMC, 1.0 mM, of CTAB at room temperature [48]. The rods are grown iteratively in three steps and the final solution must be left for several hours to attain maximal growth. The rods thus synthesized are oriented along [110] and have a penta-twinned structure. In an idealized model the side facets are all {100} (Fig. 2.3a), but in practice a mix between {100} and {110} is often found [49]. The rod termination has a pyramidal structure and consists of {111} facets (Fig. 2.3). The AR ranges between 10 to 25 and the length of a fully grown rod can be in the lower micron range [50] (Fig. 2.4). A significant shortcoming with the **P-1** protocol is that the initial yield of nanorods by shape is only about 5% before purification. It turns out there is a simple way of obtaining nanorods in high yield by a few straightforward modifications to **P-1**.

Silver-assisted protocol (P-2). In this synthesis protocol, CTAB replaces sodium citrate as the capping agent in the seed solution and silver nitrate ($AgNO_3$) is added in small amounts to the growth solution (Fig. 2.2). Nanorods are subsequently grown in a single step, yielding rods with ARs that can be precisely varied between 2 to 5 by changing the silver concentration. The overall dimensions of these rods are significantly smaller compared to the **P-1** rods, with typical rod lengths under 100 nm [50]. Furthermore, the nanorods have an octagonal cross-section and are single-crystalline rather than penta-twinned. While no broad consensus has been achieved with regards to the faceting, several studies suggest the presence of high-index prism facets such as {520} [51], or possibly a mix between such facets and {100}/{110} [52]. The termination is truncated pyramidal and exposes a mix of alternating {111} and {110} facets. Many attempts at further improvement of the silver-assisted growth protocol have been made by introducing various additives such as organic molecules and acids. A notable example is the introduction of a co-surfactant in the form of sodium oleate (NaOl), which has been observed to produce nanorods with a 99.5% yield and tunable AR [53]. Inter-

[3] Due to the quick reaction kinetics of $NaBH_4$, a lower temperature is necessary to obtain a controlled reaction.

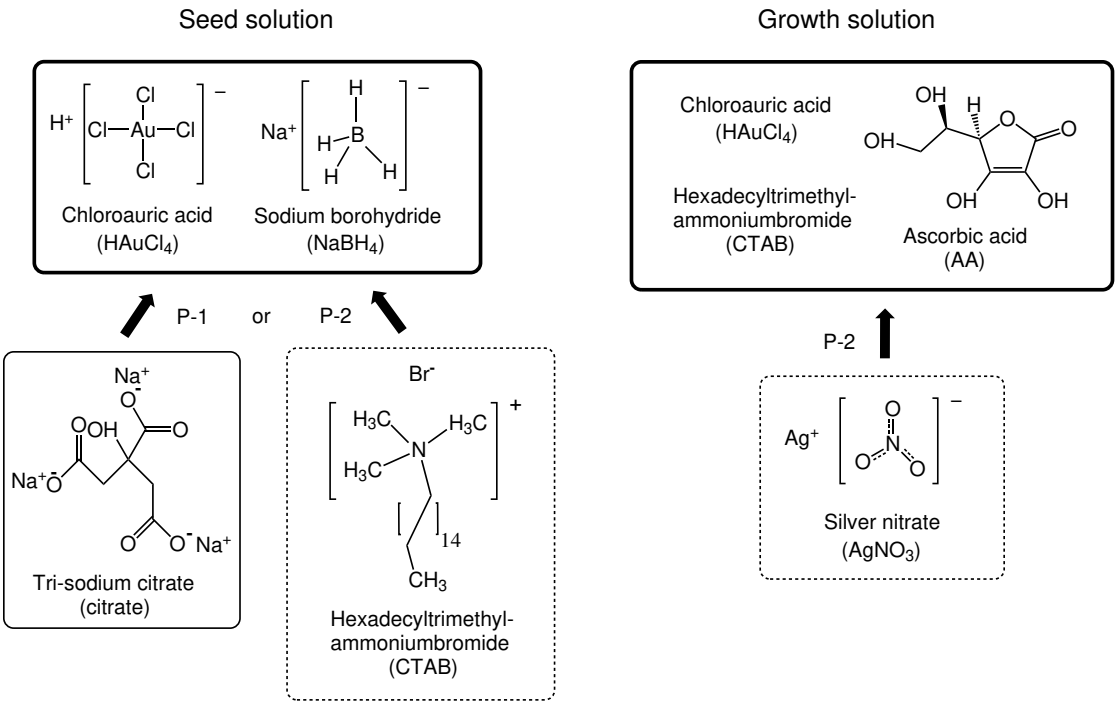

Figure 2.2: Chemical structural formulas and names of the compounds used in the seeded growth of gold nanorods via either the **P-1** or the **P-2** protocol. In a **P-2** synthesis, the CTAB replaces citrate as the stabilizing agent in the seed solution and a small amount of silver nitrate is added to the growth solution.

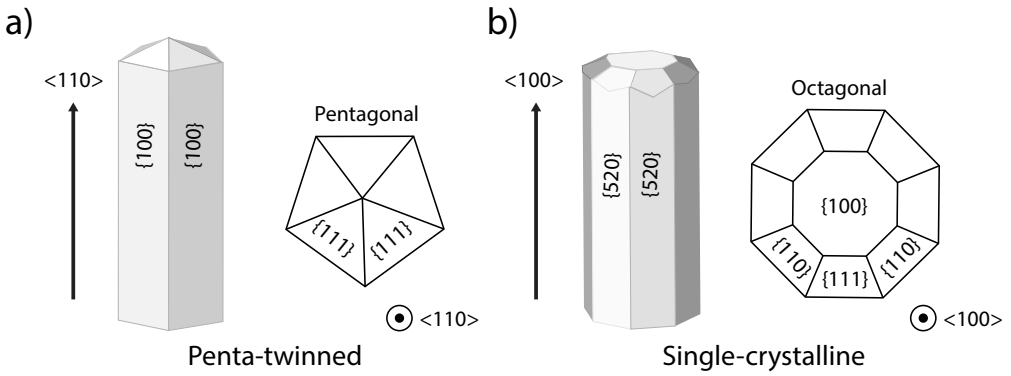

Figure 2.3: Proposed models, including cross-sections views, for the faceting of gold nanorods. a) The three-step protocol yields penta-twinned nanorods with a pyramidal termination. b) For the silver-assisted protocol, a single-crystalline structure with an octagonal cross-section is obtained. Different models have been proposed for the faceting, shown here is one based on high-index {520} prism facets.

estingly, the amount of CTAB required for this synthesis is around three times lower than what is commonly used for nanorod synthesis.

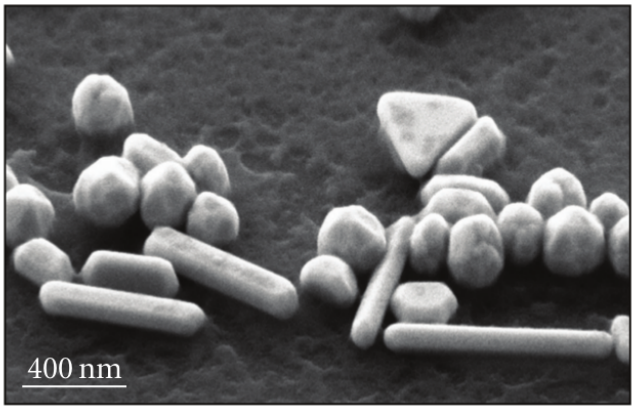

Figure 2.4: The products of a **P-1** synthesis imaged at an angle using a scanning electron microscope [54]. Note that in addition to high-aspect ratio gold nanorods, a variety of other shapes is obtained as well.

2.4 Optical properties

Much of the scientific interest in NPs stems from the fact that they can exhibit LSPR, giving rise to shape-dependent absorption and scattering. Given sufficient understanding of the correlation between particle shape and the synthesis parameters, the optical properties of the NPs can thus be controlled. As previously mentioned, the mathematical theory of interaction between light and colloidal particles started with Mie in 1908 [34], who derived analytical expressions describing the absorption and scattering of small spherical particle using classical electromagnetic theory. Only a brief summary of some especially pertinent results will be given here, for a more complete treatment the reader is referred to, e.g., [55]. The LSPR can be understood as a collective oscillation of electrons close to the surface of a NP that is excited by an external electric field (Fig. 2.5). The electrons behave similarly to a harmonic oscillator under the influence of a harmonic external force and there exists a certain resonance frequency, for which the amplitude attains a maximum[4]. Consequently, light propagating through a NP sol will be absorbed and scattered by the particles. After traversing a length L, the intensity of the light will have decayed according to the Beer-Lambert law

$$I(L) = I_0 \exp(-\rho_N C_{\text{ext}} L), \tag{2.1}$$

[4]A more apt analogy would be that of a damped driven harmonic oscillator in order to take the plasmon decay into account.

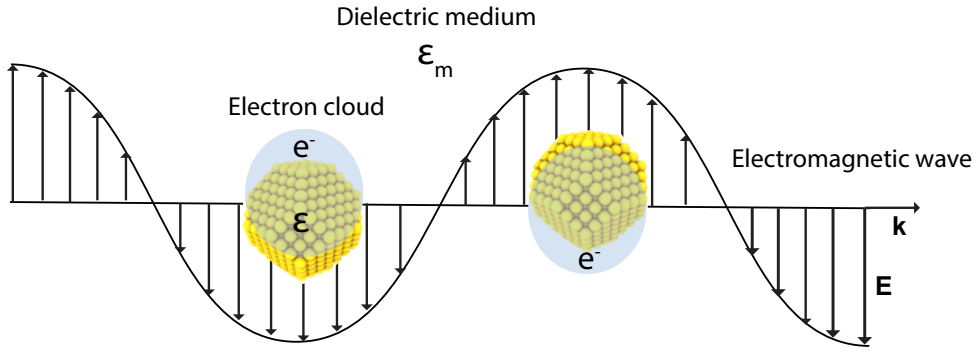

Figure 2.5: A schematic illustration of a localized surface plasmon resonance in a NP. An external electromagnetic wave with the right frequency can a excite a collective oscillation of the electron cloud near the surface of the particle.

where I_0 is the initial intensity, ρ_N the number density, and C_{ext} the so-called extinction cross section, which is defined as the sum of the absorption and scattering cross sections $C_{\text{ext}} = C_{\text{ads}} + C_{\text{sca}}$. In the case of an electromagnetic wave incident on a spherical particle of radius a and surrounded by a dielectric medium, Maxwell's equations can be solved and cross sections can be respresented in terms of infinite series. These are very laborious to compute, but in the Rayleigh-limit where the scattering particle is assumed to be smaller than the wavelength λ of the incident light simple formulas can be found. Assuming the particles are immersed in a medium with dielectric constant ϵ_m and the external field has wavenumber $k = 2\pi/\lambda$ they read

$$C_{\text{abs}} = 4\pi k a^3 \text{Im}\left\{\frac{\epsilon - \epsilon_m}{\epsilon + 2\epsilon_m}\right\} \tag{2.2}$$

and

$$C_{\text{sca}} = \frac{8\pi}{3} k^3 a^6 \left(\frac{\epsilon - \epsilon_m}{\epsilon + 2\epsilon_m}\right)^2. \tag{2.3}$$

Maximum extinction is achieved if the denominator $|\epsilon + 2\epsilon_m|$ in Eqs. (2.2) and (2.3) is minimized. Assuming $\text{Im}\{\epsilon(\omega)\}$ varies slowly around the minimum, the condition becomes

$$\text{Re}\{\epsilon(\omega)\} = -2\epsilon_m. \tag{2.4}$$

Frequencies for which this relation is satisfied are termed LSPR frequencies.

Further insight into the behavior of these oscillatory modes can be gained by assuming a free electron gas model for the conduction electrons in the metal NP. The dielectric function $\epsilon(\omega)$ is then given by

$$\epsilon(\omega) = 1 - \frac{\omega_p^2}{\omega^2 + i\gamma\omega}, \tag{2.5}$$

where ω_p is the plasma frequency and γ a damping factor. Substitution of Eq. (2.5) into the plasmon resonance condition Eq. (2.4) shows that maximum extinction will occur for frequencies that satisfy

$$\omega_{\max} = \omega_p \sqrt{2\epsilon_m + 1}. \tag{2.6}$$

From this equation it is clear that the location of the plasmon resonance depends on the dielectric environment of the particle and it is this effect that forms the theoretical basis for the use of plasmonic NPs in sensing applications. Mie's work was later extended

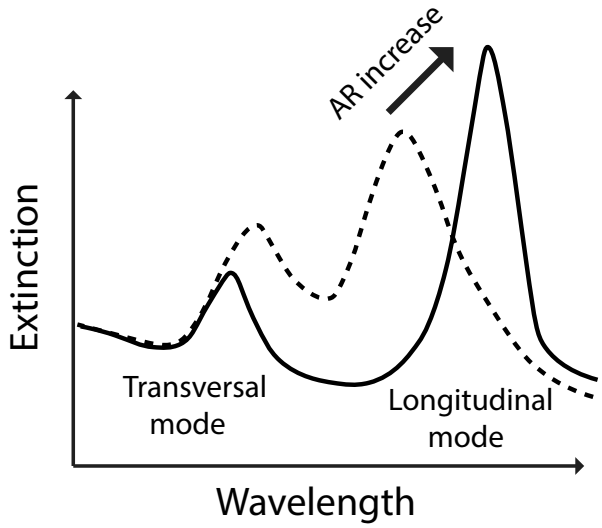

Figure 2.6: A schematic illustration of the extinction spectrum of a spheroidal NP for two different aspect ratios. The anisotropy causes the plasmonic resonance of the particle to split into a transversal and a longitudinal mode. As the aspect ratio increase the longitudinal resonance peak is redshifted, while only a small blueshift is observed for the transversal peak.

by Gans, who considered the more general case of ellipsoidal particles [35]. This result is of particular interest since an ellipsoid with axes $a > b = c$, i.e. a prolate spheroid, can be used to approximate a nanorod for which no analytical formulas are otherwise available. Note that the scattering will now depend on the orientation of the rod with respect to the incident electromagnetic wave. To describe colloidal nanorods it is thus appropriate to assume an ensemble of randomly oriented prolate spheroids and then calculate the average cross section yielding

$$\langle C_{\text{ext}} \rangle = \frac{2\pi V \epsilon_m^{3/2}}{3\lambda} \sum_{i \in \{a,b,c\}} \frac{(\epsilon / P_i)^2}{(\text{Re}\{\epsilon\} + ((1 - P_i)/P_i)\epsilon_m)^2 + \text{Im}\{\epsilon\}^2}. \tag{2.7}$$

Here, V is the volume of a spheroid and P_i are shape-dependent factors given in terms of the eccentricity $e = \sqrt{(a^2 - b^2)/a^2}$ with

$$P_a = \frac{1 - e^2}{e^2} \left(\frac{1}{2e} \log \left(\frac{1 + e}{1 - e} \right) - 1 \right) \tag{2.8}$$

and

$$P_b = P_c = \frac{1 - P_a}{2}. \tag{2.9}$$

Equation (2.7) yields extinction spectra that display two peaks. The single plasmon resonance found for a spherical particle is thus split into two resonances, corresponding to one transverse and one longitudinal mode, respectively. It is interesting to study the spectral shift of the resonances as a function of the aspect ratio AR $= a/b$ of the spheroids (Fig. 2.6). While the transverse mode is largely unaffected except for a minuscule blueshift, the longitudinal mode experiences a large redshift as the AR increases. This behavior is indeed experimentally observed for real gold nanorods, and the tunability of the longitudinal resonance peak is one of the main driving forces behind the extensive research surrounding gold nanorods as it holds the key to many applications.

3

Elements of nanoparticle modeling

Due to the vast number of different time and length scales found among processes relevant in NP modeling, there is an equally vast number of methods available for their study. Rather than giving an overview of the field [1] this chapter focuses on two specific *elements* of NP modeling relevant for the thesis. The first such element concerns the shape adopted by a NP in equilibrium and the related area of surface thermodynamics. In particular, this element forms the conceptual basis for **Papers I** and **II** and has major implications for **Paper III**. The second element concerns the description of interparticle forces, which govern colloidal stability and, by extension, deposition. This element thus represents the theoretical foundation for **Paper IV**.

3.1 Equilibrium shapes of nanoparticles

The thermodynamic equilibrium shape of a NP can be determined by means of a *Wulff construction* [57]. Consider a particle of a crystalline material M consisting of facets i with surface normals n_i with associated miller indices $\{(h_i k_i l_i)\}_{i=1,2,\ldots}$, surface free energies $\gamma_i \equiv \gamma[M(h_i k_i l_i)]$, areas A_i, and distances to the crystal center h_i. The total volume of the particle is given by

$$V = \sum_i \frac{1}{3} h_i A_i. \tag{3.1}$$

The total free energy of the particle can be decomposed into contributions from the bulk and the surface

$$G = G_{\text{bulk}}[M] + \sum_i \gamma_i A_i. \tag{3.2}$$

[1] The curious reader is referred to the review by Barnard[56].

The equilibrium shape of a particle can be found be minimizing G under the constraint of constant volume, introduced through a Lagrange multiplier [58],

$$\delta(G - \lambda V) = \delta G_{\text{bulk}}[M] + \sum_i \delta\left(\gamma_i A_i - \frac{\lambda}{3} h_i A_i\right) = 0. \tag{3.3}$$

In this equation, the first term vanishes since the volume is fixed and consequently the variation can only vanish if the terms in the summation independently vanish. This proves the Gibbs-Wulff theorem

$$h_i = \text{constant} \times \gamma_i. \tag{3.4}$$

This equation tells us that the equilibrium shape, or *Wulff shape*, is given by the set of points

$$\mathscr{W} = \{\boldsymbol{x} : \boldsymbol{x} \cdot \boldsymbol{n}_i \leq \gamma[\boldsymbol{n}_i] \text{ for all } \boldsymbol{n}_i\}. \tag{3.5}$$

The term *Wulff construction* is often used interchangeably with Wulff shape, and we shall make no distinction between the two in this text.

3.2 A thermodynamic model of adsorption

On an atomic level, *adsorption* refers to a process where any number atoms or molecules, the *adsorbates*, becomes bonded to a surface, *the adsorbent*. Adsorption is often categorized as either *chemisorption* when a chemical bond is formed between adsorbate and surface, or *physisorption* when the adsorbate is weakly bonded to the surface through van der Waals interactions. The goal of this section is to establish a thermodynamic model of adsorption that leads to a computable expression for the free energy. This enables e.g., prediction of the phase stability of a given surface system as a function of its environment, which, through the Wulff construction described above, also includes NPs. A pivotal role is played by atomistic simulation methods, which provide the total energies needed as input to the model.

Consider the interfacial region between an elemental crystal [2] M and a source of potential adsorbate molecules or atoms X. The surface $M(hkl)$ is assumed to be flat, single crystalline and initially without defects. The nature of the source, including phase, composition and properties such as dilution, is left unspecified for the moment. To account for adsorption, we write the surface free energy in Eq. (3.5) as

$$\gamma[M(hkl) : N_X X] = \gamma[M(hkl)] + \Delta\gamma[M(hkl) : N_X X], \tag{3.6}$$

where the first term on the right hand side is the clean surface free energy, and the second term represents the change in free energy induced by adsorption of N_X units

[2] The restriction to monatomic crystals is not strictly necessary but simplifies the discussion.

of X. We refer to this last term as the surface free energy of adsorption. To find an expression for this unknown quantity, we can represent a non-dissociative adsorption event (Fig. 3.1) as a reaction [3]

$$M\,(hkl) + X \rightarrow M\,(hkl)\ : X. \tag{3.7}$$

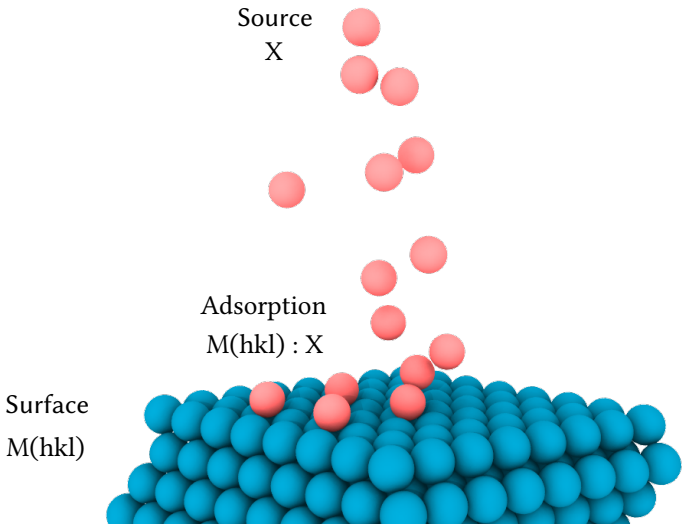

Figure 3.1: Non-dissociative adsorption on the surface of a material M in contact with a source of molecules X. This can be regarded as a reaction bringing the isolated surface and molecules together in an adsorbed state. The free energy of the reaction determines if it is endothermic or exothermic.

It is useful to generalize this reaction to allow for the possibility of a surface reconstruction. In addition to structural changes, the number of M atoms in the interfacial region can then also undergo a change $N_M \rightarrow N_M + \Delta N_M$ upon adsorption of N_X molecules. This net change can be expressed as $\Delta N_M = N_a - N_v$, where N_a is the number of adatoms and N_v is the number of vacancies. The reaction is then written in stoichiometric form as

$$N_M M(hkl) + N_X X \xrightarrow{A\Delta\gamma} (N_M + \Delta N_M) M\,(hkl)\ : N_X X - \Delta N_M M, \tag{3.8}$$

where a change in free energy per area unit $\Delta\gamma \equiv \Delta\gamma\left[M(hkl) : N_X X\right]$ has been introduced that when multiplied by the area gives the total change in Gibbs free energy ΔG

[3] In the case of dissociative adsorption when the source consists of molecules XY the dissociation must be included in the adsorption process. For example, if $X = Y$ the reaction becomes $M(hkl) + \frac{1}{2}X_2 \rightarrow M(hkl) : X$.

associated with the reaction. The change in surface free energy is obtained by taking the free energy difference of the right and left-hand side of Eq. (3.8) and dividing by the area, leading to

$$\Delta\gamma\left[M(hkl):N_X X\right] = \frac{1}{A}\left(G\left[M(hkl):N_X X\right] - G\left[M(hkl)\right] - \Delta N_M \mu\left[M\right] - N_X \mu\left[X\right]\right). \tag{3.9}$$

The terms on the right-hand side of Eq. (3.9) represent, going from left to right, the free energy of the surface with adsorbates, the free energy of the clean surface, the net change in M atoms ΔN_M times the chemical potential of the bulk $\mu\left[M\right]$, and the number of adsorbates N_X times the chemical potential of the molecules $\mu\left[X\right]$. Here, the bulk and the source are regarded as reservoirs with associated chemical potentials that measure their propensity to exchange matter with the interfacial region.

It is often convenient to write μ_X relative to a standard state $\mu^\circ\left[X\right]$,

$$\mu\left[X\right] = \mu^\circ\left[X\right] + k_B T \ln a\left[X\right]. \tag{3.10}$$

The definition of the adsorbate activity $a\left[X\right]$ in the above expression, as well as the choice of the standard state, depends on the nature of the reservoir.

3.2.1 Realization using DFT

Our thermodynamic model of adsorption on surfaces, and consequently also on NPs by virtue of Eq. (3.5), is now in principle fully defined by Eqs. (3.6), (3.9), and (3.10). Due the complicated electronic structure of the interfacial region between a crystal and an adsorbate, a quantum mechanical treatment of the system is often necessary to obtain accurate results. As discussed in the beginning of this chapter, DFT is the method of choice for such calculations. However, the energies computed using DFT correspond the electronic energy contribution in a vacuum, and hence additional models and approximations must be introduced if we are to calculate the surface free energies in Eq. (3.6).

First, we shall assume that the temperature does not deviate significantly from $T^r = 298.15\,\mathrm{K}$, i.e. room temperature. This means that vibrational contributions to the free energy are small and the free energy of a solid M_s can be well-represented by DFT. Accordingly, we prescribe the solid an absolute free energy $G[M_s] \approx E^{\mathrm{DFT}}\left[M_s\right]$. The first three terms on the right hand side of Eq. (3.9) can then be accurately determined from DFT calculations.

The remaining, and most challenging, problem pertains to the calculation of the adsorbate chemical potential appearing in Eq. (3.9). Rather than attempting a general treatment, we shall consider two different approaches and illustrate them for applications relevant to this thesis. The first approach is to combine DFT with statistical

mechanics, which will be illustrated for the case of dissociative adsorption from the gas-phase, which is relevant for **Paper I**. The second approach is to combine DFT with experimental data, which will be illustrated for aqueous halide adsorption, which is relevant for **Paper II** and to a lesser extent **Paper III**.

Gas-phase adsorption: combining DFT with statistical mechanics

The dissociative adsorption of a gas-phase dimer X_2 can be described by the reaction $M + \frac{1}{2}X_2 \longrightarrow M:X$ and the chemical potential of X appearing in Eq. (3.9) is accordingly given by $\frac{1}{2}\mu[X_2]$. If we assume X_2 behaves like an ideal gas, analytical expressions for the various free energy contributions can be derived from statistical mechanics [59]. By definition $\mu[X_2] = H[X_2] - TS[X_2]$[4] where the enthalpy can be written as

$$H[X_2] = E_{\text{elec}}[X_2] + E_{\text{ZPE}}[X_2] + \int_0^T C_P dT. \tag{3.11}$$

Here, we have separated out the electronic and the ionic ZPE contribution to the total energy, the former will be calculated using DFT. The heat capacity in the integral in Eq. (3.11) receives contributions from translational, rotational, vibrational, and electronic degrees of freedom, although the electronic contribution is typically neglected. For brevity the explicit form of these terms is not given; except for the vibrational terms, which require that the ionic vibrational energies of the system are known, they can be immediately evaluated. Additionally, as we shall see, the vibrational part of the full adsorption free energy can often be neglected, in which case no vibrational calculation is needed. The same considerations apply to the entropy, which we write relative to its value at a reference pressure conventionally chosen as $p^\circ = 1\,\text{bar}$ as

$$S[X_2](T,p) = -k_B \log\left(\frac{p}{p^\circ}\right) + \underbrace{S^\circ[X_2](T,p^\circ)}_{=S_{\text{trans}}+S_{\text{rot}}+S_{\text{vib}}} \tag{3.12}$$

Putting Eqs. (3.11) and (3.12) together, the chemical potential can be brought into the form

$$\mu[X_2](T,p) = E_{\text{elec}}[X_2] + \mu^\circ_{\text{vib}}[X_2](T) + \mu^\circ_{\text{trans,rot}}[X_2](T) - k_B T \log\left(\frac{p}{p^\circ}\right). \tag{3.13}$$

Here, the vibrational contributions, including the ZPE, have been grouped together in $\mu^\circ_{\text{vib}}[X_2]$. The remaining contributions at reference pressure, which mainly consists of a translational and rotational component, are collected in $\mu^\circ_{\text{trans,rot}}[X_2]$. We are now in

[4]Note the use of the commonly applied "lazy" notation for thermodynamic quantities Q where Q and $\partial Q/\partial N$ are both written with capital letters and the right form has to be inferred from the context.

a position to consider the full surface free energy of adsorption given in Eq. (3.9) again, where for simplicity it assumed that no reconstruction of surface takes place. We now make the approximation

$$\begin{aligned} A\Delta\gamma\left[M(hkl):N_X X\right] =& G[M(hkl):N_X X] - G[M(hkl)] - N_X\frac{1}{2}\mu[X_2] \\ \approx& E_{\mathrm{DFT}}[M(hkl):N_X X] - E_{\mathrm{DFT}}[M(hkl)] - \\ & \frac{1}{2}\left(E_{\mathrm{DFT}}[X_2] + \mu^{\circ}_{\mathrm{trans,rot}}[X_2](T) - k_B T\log\left(\frac{p}{p^{\circ}}\right)\right), \end{aligned} \tag{3.14}$$

the validity of which relies on error-cancellation of similar terms between the composite surface-adsorbate system as well as the clean surface and gas-phase molecules taken together. For instance, it can be argued that the difference in vibrational free energy between a surface with adsorbates and the clean version of that surface plus gaseous adsorbates is small [60].

Equation (3.14) provides us with a way of predicting the stability of gas-phase adsorbate structures on any crystalline surface using only 0 K DFT total energies as input, yet depends on both temperature and pressure through the two last terms.

Aqueous ion adsorption: combining DFT with experimental data

Aqueous ions are one of the more challenging types of adsorbates to describe accurately. The additional interactions and degrees of freedom introduced by the presence of the solvent make a treatment in terms of statistical mechanics difficult and cause performance issues if explicitly included in DFT calculations. This section delineates an alternative approach based on a combination of experimental data with DFT calculations. The advantage of this approach is that it allows us to completely avoid the use of DFT for solvated and ionized adsorbate states. The key idea is to find a reference bulk system that is well-described by DFT and contains the ion of interest and then use experimental free energies to connect it to the desired adsorbate state. This type of consistent combining scheme was introduced by Persson *et. al.*, who focused on the description of metal oxides [61]. The scheme presented here is, in essence, a variation of their approach. While a detailed description is given for the case of aqueous halide adsorption, extension to other ionic species is straightforward.

Experimental free energies are tabulated for a standard state under reference conditions and thus correspond to the first term in Eq. (3.10). Here, the comprehensive thermodynamic data set procured and corrected by Hunenberger and Reif [62] will be used. The conventional standard state is that of an ideal molar solution under reference conditions $P^{\circ} = 1\,\mathrm{bar}$ and $c^{\circ} = 1\,\mathrm{M}$, and the $\circ$-superscript will be used to denote values at these conditions. Note that standard values of thermodynamic quantities can still be a function of temperature, which applies in particular to μ°, while experimental

values are often tabulated only at room temperature $T^r = 298.15\,\mathrm{K}$. Accordingly, when $(c, P, T) = (c^\circ, P^\circ, T^r)$, a $\bullet$-superscript will be used instead.

Now we let X^-_{aq} for $X \in \{\mathrm{F}, \mathrm{Cl}, \mathrm{Br}, \mathrm{I}\}$, and assume that the halide solution is ideal, which means that the activity coefficient Y is unity. The activity on the right-hand side of Eq. (3.10) is then reduced to

$$a\left[X^-_{\mathrm{aq}}\right] = \mathrm{Y}\left[X^-_{\mathrm{aq}}\right] \frac{c\left[X^-_{\mathrm{aq}}\right]}{c^\circ} \approx \frac{c\left[X^-_{\mathrm{aq}}\right]}{c^\circ}. \tag{3.15}$$

The notation used in this section closely follows that of Hunenberger and Reif [62] and is succinctly summarized in Fig. 3.2. Note the distinction between reaction and formation energies. The former are free energy differences between two states, e.g., gaseous ion and solvated ion, and denoted $\Delta_r G$ while the latter measure the difference between a state and the elemental state of the halogen and are denoted $\Delta_f G$. In this context, the elemental state refers to the naturally occurring state of the ion, which for the halogens is $\frac{1}{2}X_{\mathrm{el}} = \mathrm{F_2(g)}$, $\mathrm{Cl_2(g)}$, $\mathrm{Br_2(l)}$, $\mathrm{I_2(s)}$.

The task is now to connect the experimental formation reaction energies to the total DFT energies. As we have previously argued, the energy of solids are well-described by DFT under, or close to, ambient conditions. Consequently, we can assign DFT energies to the absolute enthalpies of an alkali-halide salt MX_s and the corresponding pure alkali metal. The absolute enthalpy of a halogen X in its elemental state can now be fixed if we insist that the reactions in Fig. 3.2 all proceed with the correct experimental reaction energies

$$H^\bullet\left[X_{\mathrm{el}}\right] = E_{\mathrm{DFT}}\left[\mathrm{NaX_s}\right] - E_{\mathrm{DFT}}\left[\mathrm{Na_s}\right] - \Delta_f H^\bullet_{\mathrm{exp}}\left[\mathrm{NaX}_s\right]. \tag{3.16}$$

The absolute enthalpy of an aqueous halide ion is then simply obtained as

$$H^\bullet\left[X^-_{\mathrm{aq}}\right] = H^\bullet\left[X_{\mathrm{el}}\right] + \Delta_f H^\bullet_{\mathrm{exp}}\left[X^-_{\mathrm{aq}}\right]. \tag{3.17}$$

The standard chemical potential can now be approximated according to

$$\mu^\circ\left[X^-_{\mathrm{aq}}\right] = H^\circ\left[X^-_{\mathrm{aq}}\right](T) - TS^\circ_{\mathrm{exp}}\left[X^-_{\mathrm{aq}}\right](T) \approx H^\bullet\left[X^-_{\mathrm{aq}}\right] - TS^\bullet_{\mathrm{exp}}\left[X^-_{\mathrm{aq}}\right]. \tag{3.18}$$

The approximation here consists of neglecting the individual functional dependencies of $H^\bullet$ and $S^\bullet_{\mathrm{exp}}$ on temperature, however, an exact equality holds when $T = T^r$. It follows from Eqs. (3.10), (3.15), and (3.17) that the chemical potential at any concentration can be calculated as

$$\mu\left[X^-_{\mathrm{aq}}\right] = \mu^\circ\left[X^-_{\mathrm{aq}}\right] + k_B T \log\left(\frac{c\left[X^-_{\mathrm{aq}}\right]}{c^\circ}\right). \tag{3.19}$$

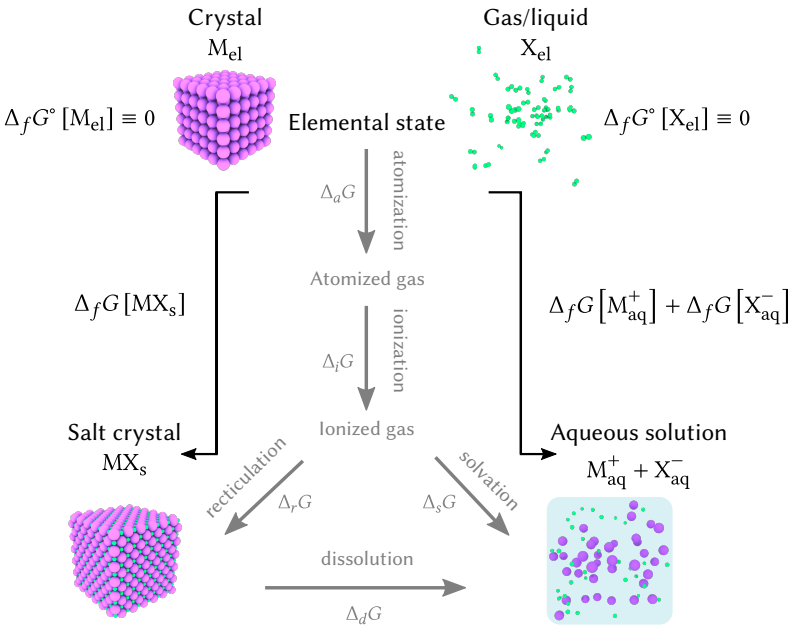

Figure 3.2: Notation for free energies and reactions relating to the formation and dissolution of alkali-halide salts. The alkali species are denoted by M and the halogens by X. In their elemental, i.e. naturally occurring state, the formation energy of a species M or X is by definition zero. Formation energies for all other states can then be measured relative to the elemental state and denoted $\Delta_f G$. In going from the elemental state to a final state, we can pass through one or more intermediate states which are connected by reaction energies $\Delta_r G$.

The final expression for the surface free energy of adsorption, see Eq. (3.14), of a halide as approximated using our combining scheme is

$$\begin{aligned}\Delta\gamma\left[M(hkl):\left(N_X X^-_{aq}\right)\right] \approx \frac{1}{A}\left(E_{\mathrm{DFT}}\left[M(hkl):N_X X\right] - \right.\\ \left. E_{\mathrm{DFT}}\left[M(hkl)\right] - N_X\left(\Phi\left[M(hkl)\right] + \mu\left[X^-_{aq}\right]\right)\right).\end{aligned} \tag{3.20}$$

Here, the DFT calculation for a charged slab implied by the first term on the right in Eq. (3.9) is avoided and replaced with the energy of a neutral system $E_{\mathrm{DFT}}\left[M(hkl):NX\right]$ using a thermodynamic cycle [63] that implies subtracting an appropriate multiple of the work function $\Phi\left[M(hkl)\right]$ of the clean surface.

It is important to note that, since we want to avoid explicit inclusion of water in the DFT calculations, all interactions between surface and solvent are neglected in the two first terms on the right-hand side of Eq. (3.20). In **Paper II**, the effect of neglecting these surface-solvent interactions is investigated by comparing the results obtained from conventional DFT without and with an implicit solvent model [64, 65].

3.3 Interparticle forces and DLVO theory

This section presents another element of modeling colloidal NPs, namely that of the forces acting between NPs themselves, rather than between the atoms on the surface of a single NP as in the previous sections of this chapter. A closely related concept is that of colloidal *stability*. In the context of colloidal science this term is not used in the thermodynamic sense of a system state that minimizes the appropriate thermodynamic potential.[5] Rather, it refers to a thermodynamically metastable state in which the system has become kinetically trapped. In this state the discrete phase remains dispersed in the continuous phase without settling or precipitating, a condition which requires the particles to obey Brownian dynamics. In practice, most colloids do settle and reach thermodynamic equilibrium over time. The rate of this process can vary dramatically, milk settles over a span of a few weeks while sols can remain intact for years.

Restricting the discussion to the case where the discrete phase consists of particles with mass m, a limiting size for the Brownian regime can be obtained [66]. Consider the distribution of particles at height h in a continuous medium of density ρ_m. In equilibrium this distribution follows Boltzmann statistics with weights determined by the gravitational potential energy

$$P(h) \propto \exp\left(-\frac{mgh}{k_B T}\right). \tag{3.21}$$

Accordingly, the distribution has a mean value $\langle h \rangle = k_B T/mg$. Assuming the particles are spherical with radius a and density ρ, they are suspended if $\langle h \rangle > 2a$, which solving for a and adjusting the density to include buoyancy yields

$$a < \left(\frac{3k_B T}{8\pi g(\rho - \rho_m)}\right)^{1/4}. \tag{3.22}$$

For, e.g., gold particles in water under ambient conditions this requirement yields an upper limit of $a \lesssim 0.5\,\mu$m. Note, however, that even if a suspension initially contains only particles of dimensions consistent with Eq. (3.21), the criterion may still be violated. This occurs if the attractive interparticle forces in the systems are stronger than their repulsive counterparts, in which case neighboring particle adhere to each other and *coalesce* or form *aggregates* that settle when they reach the limiting size.

The two most important types of interactions in colloids are vdW interactions, which are attractive, and EDL interactions, which can be either repulsive or attractive depending on the nature of the colloid. In DLVO theory, which is historically the most successful theory of colloidal stability, the total force between two colloidal particles is simply taken as the sum of the forces derived from the vdW and EDL interactions. In

[5] This would imply a phase separation between the discrete and continuous phases of the colloid.

the next two sections, we consider each of these two contributions separately and then describe in Sect. 3.3.3 how approximations for the combined DLVO interaction energy of convex bodies can be found.

3.3.1 van der Waals interactions

The driving force behind adhesion of colloidal particles comes from dispersive interactions, which are long-ranged, attractive, and present in all atomic systems. These interactions can, at least partially, be understood in terms of a semi-classical picture: quantum mechanical charge fluctuations create an instantaneous dipole in an atom A, which subsequently induces an aligned, instantaneous dipole in a neighboring atom B. The result is an interaction between the two induced dipoles AB that is always favorable and decays as $1/r^6$. The true origin of dispersive interactions is, however, purely quantum mechanical and the reader is referred to Appendix A for a more detailed discussion. Dispersive interactions are often referred to as *van-der-Waals* (vdW) interactions, although some authors use this term to also include dipole-induced dipole (Debye) and dipole-dipole (Keesom) interactions. In contrast to the dispersive interactions, the Debye and Keesom interactions can be adequately described by classical physics [67]. In this section the terms vdW and dispersive interactions are used synonymously.

The total vdW energy resulting from two interacting bodies $\mathscr{B}_1, \mathscr{B}_2$, assuming that the microscopic contribution from an interacting atomic pair follows the asymptotic $1/R^6$ form, is given by

$$U^{\mathrm{vdw}} = -\sum_{I\in\mathscr{B}_1}\sum_{J\in\mathscr{B}_2}\frac{C_6^{IJ}}{R_{IJ}^6}, \tag{3.23}$$

where C_6^{IJ} are coefficients that determine the strength of the interaction between two atoms I, J at a fixed separation R_{IJ}. In the limit of large bodies, a continuum treatment of the vdW interaction allows for the derivation of closed-form analytic expression for the total energy in a few important cases. We assume that the bodies are composed of the same atomic building blocks with number density ρ and interaction coefficient C_6. In the continuum limit Eq. (3.23) can then be cast as a double integral over the two bodies,

$$U^{\mathrm{vdw}} = -\int_{\mathscr{B}_1} d\boldsymbol{R}_1 \int_{\mathscr{B}_2} d\boldsymbol{R}_2 \rho^2 \frac{C_6}{|\boldsymbol{R}_1 - \boldsymbol{R}_2|^6}. \tag{3.24}$$

There are three important special cases for which the above integration can be carried out analytically to obtain a closed-form expression for the interaction energy. The first and simplest case is that of two infinite flat plates separated by a distance d. The interaction energy per unit area is then given by

$$u_f^{\mathrm{vdw}}(d) = -\frac{A_H}{12\pi d^2}. \tag{3.25}$$

Here, $A_h = \pi^2 \rho^2 C_6$ is known as the Hamaker constant, in honor of H. C. Hamaker who was among the first to explore dispersive interactions between macroscopic bodies. Next we consider two interacting spheres, for which Hamaker famously derived [68]

$$U_s^{\mathrm{vdw}} = -\frac{A_h}{6}\left(\frac{2a_1a_2}{d^2+2d(a_1+a_2)} + \frac{2a_1a_2}{d^2+2(a_1+a_2)+4a_1a_2} + \log\left(\frac{d^2+2d(a_1+a_2)}{d^2+2(a_1+a_2)+4a_1a_2}\right)\right), \tag{3.26}$$

for spheres of radii a_1, a_2 and shortest separation d. If we let the radius of one of the spheres tend to infinity an expression for the interaction of a single sphere with radius a with an infinite flat surface is obtained as a bonus

$$U_{sf}^{\mathrm{vdw}}(d) = -\frac{A_H}{6}\left(\frac{a}{d} + \frac{a}{d+2a} + \log\left(\frac{d}{d+2a}\right)\right). \tag{3.27}$$

3.3.2 Electrostatic interactions

In order to stabilize the colloidal particles against aggregation or coalescence the net inter-particle forces must be repulsive. One way to stabilize the particles is via so-called electrostatic stabilization[6], where the surface charge of the particles is tuned so that they repel each other.

There are many pathways through which a particle surface can acquire a net charge. These include, for instance, adsorption of a charged species, dissociation of a surface species into charged fragments as well as the build-up of a positive or negative excess of electrons at the surface. Once the surface has become charged, oppositely charged species are attracted towards it forming an electric *double layer*.

Limiting the discussion to colloidal particles in ionic solutions, which is the setting relevant for wet-chemical synthesis processes, an illustrative derivation of the electrostatic interaction between two charged spherical particles is provided below. Detailed accounts can be found in elementary textbooks on electrolyte solutions [69]. The double layer charge distribution gives rise to an electric surface potential ϕ that can be obtained from the Poisson equation

$$\Delta\phi(\boldsymbol{r}) = -\rho(\boldsymbol{r}). \tag{3.28}$$

In equilibrium, the concentrations of each ionic species j with bulk concentration n_j^0 and charge q_j follow Boltzmann statistics. Combined with Eq. (3.28) this results in the

[6] Another option is *steric stabilization*, where polymers are grafted onto the particle surface. As two particles approach each other, an overlap region is created in which the confinement of the polymers leads to a loss of configurational entropy that manifests as a repulsive force.

PB equation

$$\frac{d^2\phi}{dx^2} = -\frac{1}{\epsilon_0\epsilon_r}\sum_j q_j c_j^\infty e^{-q_j\phi/(k_BT)}, \tag{3.29}$$

where $\epsilon = \epsilon_0\epsilon_r$ and ϵ_r is the dielectric constant of the medium. Since the electric potential also appears in the Boltzmann factors in Eq. (3.29), the PB equation is non-linear and no closed-form analytic solutions are available. A common approximation is the *Debye-Hückel linearization*, obtained by Taylor expanding the Boltzmann factors to second order yielding the LPBE

$$\Delta\phi(\boldsymbol{r}) = \kappa^2\phi(\boldsymbol{r}). \tag{3.30}$$

Here, the *Debye screening length*

$$\kappa^{-1} = \sqrt{\frac{\epsilon k_B T}{\sum_j n_j^0 q_j^2}}, \tag{3.31}$$

was introduced, which provides a measure of the effective range of the electrostatic interaction in an electrolyte. The LPBE can be solved exactly for some simple systems, the most important example of which is an electrolyte surrounded by two infinite parallel plates at separation d. Hogg, Healy, and Fuerstenau [70] showed, assuming constant surface potentials ϕ_1 and ϕ_2 on the plates, that an analytic expression can be derived not only for the electrostatic potential, but also for the total interaction energy per unit area

$$u_f^{\mathrm{edl}}(d) = \frac{\epsilon_0\epsilon_r\kappa}{2}(\phi_1^2+\phi_2^2)\left(1-\coth(\kappa d)+\frac{2\phi_1\phi_2}{\phi_1^2+\phi_2^2}\operatorname{cosech}(\kappa d)\right). \tag{3.32}$$

This is often referred to as the Hogg-Healy-Fuerstenau formula [70]. The reason that the two-plate system is of special importance is because it allows for the derivation of approximate interaction expressions for arbitrary convex geometries using the *Derjaguin approximation*, which will be discussed in the next section. First, we remark that the error in the electric potential introduced as a result of using the LPBE is $\mathcal{O}(\phi^3)$ for symmetric electrolytes, i.e. if the valences of the anions and cations are equal $z_1 = z_2$, but $\mathcal{O}(\phi^2)$ if the electrolyte is asymmetric ($z_1 \neq z_2$). To see the significance of this, we observe that from Eq. (3.29) the range of validity for the linearization is $q\phi \ll k_BT$, which for monovalent ions in room temperature translates to $\phi \ll 25\,\mathrm{mV}$. Now, for symmetric electrolytes it has been noted that the LPBE yields decent results even if $\phi \approx 25\,\mathrm{mV}$ [70], but due to the increased approximation error the same cannot be said for the asymmetric case. Hence, in practice one is often forced to solve the non-linear PB equation for asymmetric electrolytes, which is the case, e.g., in **Paper IV**.

Even when the LPBE is not valid, however, it is still straightforward to obtain the two-plate interaction energy if the PB equation can be solved numerically. In this case,

we note that the disjoining-pressure Π of the plates is given by the sum of the osmotic and electromagnetic pressures according to

$$\Pi(d) = k_B T \sum_j c_j^0 \left(e^{-q_j \phi_d/(k_B T)} - 1\right) - \frac{\epsilon_0 \epsilon_r}{2} \frac{d^2 \phi_d}{dx^2}. \tag{3.33}$$

The total total interaction energy can subsequently be obtained by integration

$$u_f^{\text{edl}}(d) = \int_{s=d}^{\infty} \Pi(s) ds. \tag{3.34}$$

3.3.3 Surface element integration

As alluded to in the previous section, the Derjaguin approximation can be used to obtain the total DLVO interaction energy between two arbitrary convex bodies, given that the interaction energy for two corresponding infinite, parallel plates with the same boundary conditions can be calculated at any separation. More precisely, given the distance of closest separation D of two arbitrary convex bodies $\mathscr{B}_1, \mathscr{B}_2$, can be approximated as

$$U(D) = g(\boldsymbol{\kappa}_1, \boldsymbol{\kappa}_2) \int_{s=D}^{\infty} u_f^{\text{tot}}(s) ds \tag{3.35}$$

where $u_f^{\text{tot}} = u_f^{\text{vdw}} + u_f^{\text{edl}}$ is the total DLVO energy of the two-plate system (see Eqs. (3.25) and (3.34)) and g is a geometric factor that depends on the principal curvatures $\boldsymbol{\kappa}_1, \boldsymbol{\kappa}_2$ of the two surfaces $\mathscr{S}_{1,2} = \partial \mathscr{B}_{1,2}$. Despite the usefulness of the Derjaguin approximation in finding analytic expressions for the DLVO interaction between a wide range of important geometries [67], it suffers from critical limitations. More precisely, the distance of closest approach and characteristic range of the DLVO interaction must be small compared to the radii of curvature of both the surfaces [71].

For the specific case of a convex body interacting with an infinite flat plate, a more accurate method of obtaining the interaction energy was proposed by Bhattacharjee and Elimelech [72] termed *SEI*. Indeed, it was shown that using SEI, the exact vdW interaction (Eq. (3.27)) was recovered and that the EDL interaction calculated based on the Hogg-Healy-Fuerstenau solution Eq. (3.32) matched results from finite element solutions of the PB equation within the linear regime.

To formulate the SEI method, we consider an infinite flat plate $\mathscr{A}$ and a convex body $\mathscr{S}$, with corresponding surface elements $d\boldsymbol{A} = \boldsymbol{k} dA$ and $d\boldsymbol{S} = \boldsymbol{n} dS$, where $\boldsymbol{k}$ and $\boldsymbol{n}$ are the respective surface normals. Contributions to the total interaction energy are then computed for each surface element of $\mathscr{S}$ as $dU = d\boldsymbol{S} \cdot \boldsymbol{k} u_f(s)$, where s is the local separation between $d\boldsymbol{S}$ and $\mathscr{A}$. Accordingly, the total interaction energy is

$$U(D) = \int_{\mathscr{S}} d\boldsymbol{S} \cdot \boldsymbol{k} u_f^{\text{tot}}(s) = \int_{\mathscr{A}} dA \frac{\boldsymbol{n} \cdot \boldsymbol{k}}{|\boldsymbol{n} \cdot \boldsymbol{k}|} u_f^{\text{tot}}(s) \tag{3.36}$$

where D is the distance of closest approach between $\mathscr{S}$ and $\mathscr{A}$. Subsequent work by the same authors extended the SEI method to the more general case of two convex bodies [73], and while it still constitutes an improvement over the Derjaguin approximation, the predicted energies are in this more general case only accurate when the characteristic interaction range is short. For instance, the exact Hamaker expression for the vdW interaction between two spheres given in Eq. (3.26) is not reproduced but rather the SEI value tend towards the exact value as the ratio between the radii increases, i.e. when approaching the sphere-plate limit. The SEI method is the basis of the model implemented in **Paper IV** to evaluate the efficacy of pre-patterned Ni structures on a SiO_2 substrate in attracting citrate-stabilized Au NPs.

4

First-principles calculations

"But, gentlemen, that's not physics."

Ceylonese parrot nominated as chairman for all seminars on quatum mechanics in Göttingen 1927.

All properties of a system of interacting, non-relativistic particles are in principle determined by its many-body state $|\Phi(t)\rangle$, which is obtained as a solution to the time-dependent Schrödinger equation

$$i\hbar\frac{\partial}{\partial t}|\Phi(t)\rangle = H|\Phi(t)\rangle, \tag{4.1}$$

where H is the Hamilton operator of the system. The spectrum of this operator, defined by the eigenvalue equation

$$H|\Psi\rangle = E|\Psi\rangle, \tag{4.2}$$

corresponds to the allowed energies E of the system. Equation (4.2) is often referred to as the time-independent Schrödinger equation. The eigenstates $|\Psi\rangle$ may be used as a basis for an expansion of an arbitrary many-body state, but for many applications it is sufficient to know the ground state of the system i.e. the lowest eigenvalue E_0 of H and its associated eigenstate $|\Psi_0\rangle$.

For a system consisting of N electrons and M atomic nuclei, the position-space representation of the Hamilton operator in Hartree atomic units ($\hbar = e = m_e = 4\pi\epsilon_0 = 1$) is given by

$$H = \overbrace{-\frac{1}{2}\sum_{i}^{N}\nabla_i^2}^{T} + \overbrace{\sum_{i=1}^{N}\sum_{j>i}^{N}\frac{1}{|\boldsymbol{r}_i-\boldsymbol{r}_j|}}^{V_{\text{int}}} \overbrace{-\sum_{i=1}^{N}\sum_{I=1}^{M}\frac{Z_i}{|\boldsymbol{r}_i-\boldsymbol{R}_I|}}^{V_{\text{ext}}} \underbrace{-\frac{1}{2}\sum_{I=1}^{M}\frac{\nabla_I^2}{M_I}}_{T_{\text{ion}}} + \underbrace{\sum_{I=1}^{M}\sum_{J>I}^{M}\frac{Z_I Z_J}{|\boldsymbol{R}_I-\boldsymbol{R}_J|}}_{E_{\text{nn}}} \tag{4.3}$$

where $M_I, Z_I, \boldsymbol{R}_I$ denote the mass, charge and position of the nuclei, respectively, and $\boldsymbol{r}_i$ are the positions of the electrons. Exact solutions to Eq. (4.2) are only possible for 1-body systems or 2-body systems that can be reduced into 1-body problems, as is the case of an isolated hydrogen atom. In all other cases, we must resort to approximations and numerical solutions. If the approximations giving rise to a certain method are of such nature that the resulting equations are free from adjustable physical parameters, the method is customarily referred to as an *ab initio* or *first-principles* method.

A common approximation for many methods seeking to solve Eq. (4.2) for the Hamilton operator in Eq. (4.3) is to make use of the fact that the nuclei are much heavier than the electrons. For the electrons this means that they see the nuclei as charges frozen in their instantaneous location, hence the nuclear kinetic energy term can be dropped and the ion-ion repulsion E_{nn} simply amounts to a constant shift of the Hamilton operator. This is known as the *Born-Oppenheimer approximation* [74] and allows us to write a simplified electronic Hamilton operator

$$H_{\text{e}} = T + V_{\text{int}} + V_{\text{ext}}. \tag{4.4}$$

With the spin variables suppressed, the time-independent Schrödinger equation for the electrons now reads

$$H_e\Psi_e(\{\boldsymbol{r}_i\};\{\boldsymbol{R}_I\}) = E_e\Psi_e(\{\boldsymbol{r}_i\};\{\boldsymbol{R}_I\}) \tag{4.5}$$

and the total energy is $E_{\text{tot}} = E_e + E_{nn}$. Similarly, we can write a separate Schrödinger equation for the nuclei, which can then be regarded as moving in a mean-field generated by the electrons. Here, a full quantum mechanical treatment is often not necessary and the nuclei can be regarded as classical particles moving in the potential $E_{\text{tot}}(\{\boldsymbol{R}_I\})$ obtained by solving the electronic problem Eq. (4.5) and often referred to as the *potential energy surface*. The force on a nuclei I is given by

$$\boldsymbol{F}_I = -\frac{\partial}{\partial \boldsymbol{R}_I}E_{\text{tot}}(\{\boldsymbol{R}_I\}) = -\left\langle\Psi\left|\frac{\partial H}{\partial \boldsymbol{R}_I}\right|\Psi\right\rangle - \underbrace{E\frac{\partial}{\partial \boldsymbol{R}_I}\langle\Psi|\Psi\rangle}_{=0 \text{ if basis is complete}}. \tag{4.6}$$

This is known as the *Hellmann-Feynman* theorem and evaluation of the first term in Eq. (4.6) shows that the forces on the ions are simply the electrostatic forces due to the electronic charge distribution. Numerical solutions to the Schrödinger equation are typically based on a basis expansion of the wavefunction (Sect. 4.1.5), however, and only a finite number of such functions can be included. In this case, the derivative in the second term in Eq. (4.6) is not zero if the basis functions depend on the ionic positions. As a result the ions experience so-called *Pulay forces* that need to be corrected for according to Eq. (4.6).

Despite greatly simplifying the original problem, Eq. (4.4) further theoretical development is required to obtain equations can be solved, at least numerically.

4.1 Density functional theory

Density functional theory (DFT) is one of the cornerstones of modern computational materials physics and provides a way of solving the Schrödinger equation to a high degree of accuracy with an efficiency that makes calculations involving several hundreds of atoms tractable on modern supercomputers. As alluded to by the name, the electronic density plays a fundamental role in this theory and is defined in terms of the many-body electronic wavefunction from Eq. (4.4) as

$$n(\boldsymbol{r}) = \int d\boldsymbol{r}_2 \dots d\boldsymbol{r}_N \, |\Psi(\boldsymbol{r}, \boldsymbol{r}_2, \dots, \boldsymbol{r}_N)|^2 \tag{4.7}$$

where the subscript has been dropped from Ψ_e and the parametric dependence on the nuclear coordinates has been suppressed.

4.1.1 The Hohenberg-Kohn theorems

The theoretical foundation of DFT rests on the shoulders of two theorems proved by Hohenberg and Kohn (HK) in 1964 [75]. We shall be content with giving a concise summary of them here, for a more detailed account readers are referred to one the many textbooks covering the topic [76, 77]. For a stationary, interacting, non-degenerate system of electrons there is a one-to-one mapping between V_{ext}, $|\Psi_0\rangle$ and $n(\boldsymbol{r})$. Consequently, the ground state is a *functional* of the ground state density, which is denoted $|\Psi[n]\rangle$. This functional is unique and takes the same form regardless of V_{ext}, provided that V_{int} does not change. This implies in turn that the ground state expectation value of any observable is also a functional of the density

$$O[n] = \langle \Psi[n] | \, O \, | \Psi[n] \rangle \, . \tag{4.8}$$

Of particular interest is the ground state energy

$$E[n] = \langle \Psi[n] | \, H_e \, | \Psi[n] \rangle = \langle \Psi[n] | \, T + V_{\text{int}} \, | \Psi[n] \rangle + E_{\text{ext}} \tag{4.9}$$

where the the external energy functional

$$E_{\text{ext}}[n] = \int d\boldsymbol{r} \, n(\boldsymbol{r}) V_{\text{ext}}(\boldsymbol{r}). \tag{4.10}$$

has been defined. The total energy functional in Eq. (4.9) can be shown to obey a variational principle with a minimum corresponding to the true ground state density, i.e.

$$E[n] < E[n'] \, , \forall n' \neq n \tag{4.11}$$

An appealing feature of these results is that the unwieldy many-body wavefunction in bypassed favor of the electronic ground state density, a scalar function of only three variables. Note however, that the HK theorems are pure existence theorems and do not contain a recipe for constructing an explicit expression for $E[n]$ that would allow for determination the ground-state energy and other observables.

4.1.2 Kohn-Sham theory

Kohn-Sham (KS) theory provides us with a way of leveraging the Hohenberg-Kohn theorems to derive a practical scheme for determining the ground state density of a system [78]. It rests on the non-trivial assumption that a system of interacting electrons can be mapped onto a system of fictitious, non-interacting electrons in such a way that the ground-state electron density is the same for the two systems. This new system is typically referred to as the KS auxiliary system and its existence has not been proved for the general case; rather it is typically justified from a practical perspective by the remarkable success of KS theory in predicting many material properties. Since the KS system is non-interacting, it can be described by a set of single-particle, Schrödinger-like equations

$$\underbrace{\left[-\frac{1}{2}\nabla^2 + V_{\text{KS}}(\boldsymbol{r}) \right]}_{\equiv H_{\text{KS}}} \Psi_i(\boldsymbol{r}) = \epsilon_i \Psi_i(\boldsymbol{r}). \tag{4.12}$$

The density is then simply $n(\boldsymbol{r}) = \sum_i f_i |\Psi_i(\boldsymbol{r})|^2$, where f_i is the occupation number of orbital i. Here, V_{KS} is an effective potential for which a useful expression can be derived by decomposing the energy functional for the KS system according to

$$E_{\text{KS}} = T_s[n] + E_{\text{H}}[n] + E_{\text{xc}}[n] + E_{\text{ext}}[n] \tag{4.13}$$

where the very first term is the kinetic energy functional

$$T_s[n] = -\frac{1}{2}\sum_i f_i \Psi_i(\boldsymbol{r})\nabla^2\Psi_i(\boldsymbol{r}). \tag{4.14}$$

The interactions of the original many-body problem, other than those coming from the external potential, are reflected by the interacting KS density in the other two terms E_H and E_{xc}. The first of these terms is the Hartree energy functional

$$E_H[n] = \frac{1}{2}\int d\boldsymbol{r}\, d\boldsymbol{r}'\, \frac{n(\boldsymbol{r})n(\boldsymbol{r}')}{|\boldsymbol{r}-\boldsymbol{r}'|}. \tag{4.15}$$

The last term E_{xc} in Eq. (4.13) is known as the *exchange-correlation* functional and is defined to contain all many-body effects such that the ground state density of the KS system will indeed be equal to that of the original interacting system. By using the Hohenberg-Kohn variational principle for E_{KS}, a set of independent electron equations of the form Eq. (4.12) is obtained with

$$V_{\text{KS}} = \underbrace{\int d\boldsymbol{r}'\, \frac{n(\boldsymbol{r}')}{|\boldsymbol{r}-\boldsymbol{r}'|}}_{\equiv V_H(\boldsymbol{r})} + \underbrace{\frac{\delta E_{\text{xc}}}{\delta n(\boldsymbol{r})}}_{\equiv V_{\text{xc}}(\boldsymbol{r})} + V_{\text{ext}}(\boldsymbol{r}). \tag{4.16}$$

Once the KS equations in (4.12) have been solved the ground state energy can be calculated as

$$E_0 = \sum_i f_i\epsilon_i - E_H[n(\boldsymbol{r})] - \int d\boldsymbol{r}\, n(\boldsymbol{r})V_{\text{xc}}(\boldsymbol{r}) + E_{\text{xc}}[n]. \tag{4.17}$$

4.1.3 Approximating the exchange-correlation functional

The ground state energy as calculated from the KS system as in Eq. (4.17) is exact provided that exact expressions for all terms in Eq. (4.16) are known. This is, however, not the case for the exchange-correlation functional E_{xc}, which was defined to capture all the many-body effects not included by the other terms. E_{xc} constitutes the major source of approximation in DFT.

Short of neglecting E_{xc} altogether, the simplest approach we can take is the *local density approximation* (LDA), in which a differential volume $d\boldsymbol{r}$ is assumed to give a contribution to the total exchange-correlation energy equal to the energy density of a homogeneous electron gas (HEG) having density $n(\boldsymbol{r})$ so that

$$E_{\text{xc}}^{\text{LDA}} = \int d\boldsymbol{r}\, n(\boldsymbol{r})\epsilon_{\text{xc}}^{\text{LDA}}[n(\boldsymbol{r})], \tag{4.18}$$

where $\epsilon_{\text{xc}}^{\text{LDA}}$ is the HEG energy density. Note that this expression is purely *local* in the sense that $E_{\text{xc}}^{\text{LDA}}$ is the sum of point-wise evaluated contributions. A natural extension

is to consider also variations in the density i.e., make use of the gradient $|\nabla n(\boldsymbol{r})|$ and possibly higher order derivatives, referred to as a *generalized-gradient approximation* (GGA)

$$E_{\mathrm{xc}}^{\mathrm{GGA}} = \int d\boldsymbol{r}\, n(\boldsymbol{r}) \epsilon_{\mathrm{xc}}^{\mathrm{GGA}}[n(\boldsymbol{r}), |\nabla n(\boldsymbol{r})|, |\nabla^2 n(\boldsymbol{r})|, \ldots]. \tag{4.19}$$

Such approximations are termed *semi-local* to indicate that the contributions, while still evaluated at a point, take the infinitesimal environment into account through the inclusion of density derivatives. A popular GGA-type method is the Perdew-Burke-Ernzerhof (PBE) functional [79], which takes into account first-order variations of the density.

4.1.4 Dispersion-corrections

A major shortcoming of local or semi-local exchange-correlation functional is that they do not account for dispersive interactions. These interactions are inherently non-local and thus connect the electron density at different points in space. Therefore, from the functional forms Eqs. (4.18) and (4.19) of LDA and GGA-type functionals it is apparent that they by definition cannot include non-local effects.

A simple and efficient approach to include dispersive interactions is the DFT-D method [80], which in its most basic form introduces an interatomic pair potential with the correct asymptotic $1/r^6$-form to the total DFT energy E_0 in Eq. (4.17),

$$E_0^{\text{DFT-D}} = E_0 + \sum_{IJ} \frac{C_6^{IJ}}{R_{IJ}^6}. \tag{4.20}$$

The C_6-coefficients appearing in this equation are fitted to dispersive interactions between molecules calculated using quantum-chemistry methods. There are many drawbacks to this method [81]: the C_6-coefficients are agnostic to the local environment, there is no screening, only the first order correction to the vdW energy is taken into account (see Appendix A), and the correct short-range vdW behavior is not reproduced. While the two latter deficiencies are addressed to some extent in later incarnations of the method [82, 83], it is still fundamentally semi-empirical in nature since it relies on the availability of accurate values for the C_6-coefficients. For many systems, in particular molecular ones, this level of treatment may prove sufficient, but since vdW interaction are typically weak even small inaccuracies can yield results that are qualitatively wrong. Several other dispersion-correction methods are available that suffer these drawbacks to varying degrees [84–86].

An ab initio approach to the problem is provided by the van der Waals density functional (vdW-DF) framework. The underlying theory has a long history and is quite involved, hence only a brief overview is given here and the curious reader is referred

to more detailed accounts [87, 88]. The vdW-DF framework has given birth to a family of functionals that can be written in the general form

$$E_{\mathrm{xc}}^{\text{vdW-DF}}[n] = E_x^{\mathrm{GGA}}[n] + E_c^{\mathrm{LDA}}[n] + E_c^{\mathrm{nl}}[n]. \tag{4.21}$$

Each family member is thus the sum of the exchange part of a suitably chosen GGA companion functional, local LDA correlation and a non-local correlation functional. The latter functional can be written

$$E_c^{\mathrm{nl}}[n] = \frac{1}{2}\int d\boldsymbol{r}\, d\boldsymbol{r}'\, n(\boldsymbol{r})K(\boldsymbol{r},\boldsymbol{r}')n(\boldsymbol{r}') \tag{4.22}$$

and accounts for the dispersive interactions. Here, the integration kernel $K(\boldsymbol{r},\boldsymbol{r}')$ contains information about how strongly two density regions interact depending on their spatial separation and the asymmetry of their response. While approximations are made in deriving Eqs. (4.21) and (4.22), no adjustable parameters with physical significance, akin to the C_6 coefficients of the DFT-D method, are introduced and hence vdW-DF constitutes a genuine first-principles method. It should also be clarified that while the larger vdW-DF framework accounts for many-body dispersion effects, approximations made in deriving the actual functional Eq. (4.22) limit the inclusion of such effects to length scales corresponding to typical binding distances. This is easily overlooked since Eq. (4.22) has the form of a double summation and the information about screening is effectively hidden in the kernel [88].

A practical problem encountered when implementing a vdW-DF functional is that straightforward numerical evaluation of the six-dimensional integral Eq. (4.22) is much too costly. To bring the computational effort required to a manageable level, a method due to Román-Pérez and Soler can be employed where the kernel is effectively tabulated in terms of two parameters. The non-nocal energy can subsequently be calculated by fast Fourier transforms and three-dimensional integrations [89]. This is the subject of **Paper II**, which describes a reference implementation in the form of a `C`-library that make vdW-DF functionals available to an interfacing DFT code.

Two of most most prolific vdW-DF family members are vdW-DF1 [90]

$$E_{\mathrm{xc}}^{\text{vdW-DF1}}[n] = E_x^{\mathrm{revPBE}}[n] + E_c^{\mathrm{LDA}}[n] + E_c^{\mathrm{nl}(1)}[n], \tag{4.23}$$

and vdW-DF2 [91]

$$E_{\mathrm{xc}}^{\text{vdW-DF2}}[n] = E_x^{\mathrm{PW86r}}[n] + E_c^{\mathrm{LDA}}[n] + E_c^{\mathrm{nl}(2)}[n]. \tag{4.24}$$

Note that the non-local correlation functionals used above differ slightly with regards to an underlying approximation and are consequently accompanied by different exchange functionals. For vdW-DF1 the conventional choice is the revised version of PBE by Zhang-Yang (revPBE) [92] and for vdW-DF2 it is the refitted Perdew-Wang functional (PW86r) [93]. A more recent addition to the family is vdW-DF-cx [94]

$$E_{\mathrm{xc}}^{\text{vdW-DF-cx}}[n] = E_x^{\text{LV-PW86r}}[n] + E_c^{\mathrm{LDA}}[n] + E_c^{\mathrm{nl}(1)}[n]. \tag{4.25}$$

The new feature is an exchange companion termed LV (Langreth-Vosko)-PW86r that utilizes concepts from the vdW-DF framework also for the description of the exchange contribution. In **Paper I**, the use of vdW-DF-cx was crucial in obtaining accurate results for inter-chain and surface-chain vdW interactions of thiols on gold, while maintaining a good description of the surface. Indeed, it has been demonstrated that vdW-DF-cx yields excellent agreement with experimental values for many bulk properties of a large set of solids [95].

4.1.5 Solving the Kohn-Sham equations

Given a suitable approximation for the exchange-correlation functional the KS equations (4.12) remain to be solved, a formidable challenge in itself. From Eqs. (4.12) and (4.16) it is seen that V_{KS}, which naturally must be known in order for the KS equations to be completely specified, depends on the density, which in turn cannot be known before the KS equations have been solved. To progress from this circular situation, a *self-consistent* approach must be taken in solving the equations. This means that a reasonable starting density is constructed, usually from atomic orbitals, and used to determine V_{KS} so that the KS equations may be solved. The states $|\Psi_i\rangle$ thus obtained are then combined into a new density and the whole process is repeated iteratively until convergence, according to some judiciously chosen criterion, is achieved.

To actually solve the KS set of single-particle equations Eq. (4.12), a common approach is to expand the orbitals in terms of a basis $\mathscr{B}$ for the Hilbert space

$$|\Psi\rangle = \sum_b \langle b|\Psi\rangle\, |b\rangle\,, \tag{4.26}$$

where the sum extends over all $b \in \mathscr{B}$ and the orbital index i has been dropped for convenience. Substituting this expressions into Eq. (4.12) and multiplying from the left with $|b'\rangle$ yields

$$\sum_b \langle b' \,|\, H_{\mathrm{KS}} \,|\, b\rangle \langle b|\Psi\rangle = \epsilon \sum_b \langle b'|b\rangle \langle b|\Psi\rangle\,, \tag{4.27}$$

which has the form of a generalized matrix eigenvalue problem

$$\boldsymbol{H}_{\mathrm{KS}}\boldsymbol{\Psi} = \epsilon \boldsymbol{S}\boldsymbol{\Psi}, \tag{4.28}$$

where

$$\begin{aligned} \boldsymbol{H}_{\mathrm{KS}} &= [\langle b' \,|\, H_{\mathrm{KS}} \,|\, b\rangle]_{b,b'\in\mathscr{B}} \\ \boldsymbol{\Psi} &= [\langle b|\Psi\rangle]_{b\in\mathscr{B}} \\ \boldsymbol{S} &= [\langle b' \,|\, b\rangle]_{b,b'\in\mathscr{B}} \end{aligned}\,.$$

By only including a finite number of elements in the basis expansion (4.26) the problem can be solved numerically and if the basis set is furthermore orthogonal, the overlap matrix $\boldsymbol{S}$ reduces to the identity matrix and an ordinary eigenvalue problem is obtained. What basis set to choose depends on the problem at hand, since even if any orthonormal set can in principle be used, the resulting computational effort can vary significantly.

4.1.6 Periodic systems and plane waves

For a system with periodic boundary conditions, such as a crystal, the wavefunction can be expanded in terms of plane waves and Bloch's theorem asserts that for energy eigenfunctions this expansion takes the form [96]

$$|\Psi_{\boldsymbol{k}}\rangle = \sum_{\boldsymbol{G}} c_{\boldsymbol{k}+\boldsymbol{G}} \, |\boldsymbol{k}+\boldsymbol{G}\rangle \,, \tag{4.29}$$

where $\boldsymbol{G}$ is a reciprocal lattice vector and $|\boldsymbol{k}\rangle$ represents a plane wave state, i.e. $\langle \boldsymbol{r}|\boldsymbol{k}\rangle \sim e^{i\boldsymbol{k}\cdot\boldsymbol{r}}$. The wave vector $\boldsymbol{k}$ is continuous and arbitrary but can be restricted to lie in the first Brillouin zone. Note that for molecules and other systems with no inherent periodicity, it can be artificially introduced by periodically inserting mirror images of the system with enough separation that any interaction between them effectively vanishes.

Using the notation for the matrix elements introduced in the previous section, the overlap matrix $\boldsymbol{S}$ is equal to the unit matrix since plane waves are orthogonal. Furthermore, given the Fourier expansion for the periodic potential

$$V_{\mathrm{KS}}(\boldsymbol{r}) = \sum_{\boldsymbol{G}} v_{\boldsymbol{G}} e^{i\boldsymbol{G}\cdot\boldsymbol{r}}, \tag{4.30}$$

the matrix elements of the KS Hamilton operator can be written

$$\langle \boldsymbol{k}+\boldsymbol{G}' \,|\, H_{\mathrm{KS}} \,|\, \boldsymbol{k}+\boldsymbol{G}\rangle = \frac{1}{2} \, |\boldsymbol{k}+\boldsymbol{G}|^2 \, \delta_{\boldsymbol{G}\boldsymbol{G}'} + v_{\boldsymbol{G}-\boldsymbol{G}'}. \tag{4.31}$$

The expansion is truncated by choosing a kinetic energy cutoff for the plane waves according to $|\boldsymbol{k}+\boldsymbol{G}| = \sqrt{2E_{\mathrm{cut}}}$, thus providing a simple, systematic way of improving the accuracy in a DFT calculation. Other advantages of plane wave expansions include the absence of Pulay forces[1], numerical efficiency due to the use of fast Fourier transforms, and the orthogonality of the basis.

The major issue with plane wave expansions lies in the description of the atomic core region, where the kinetic energy of the electrons is high and the wave function varies rapidly. This implies that, due to their delocalized nature, an extremely high number of plane waves would be required to accurately represent the electronic density in this

[1] This is only true as long as the cell metric does not change and thus Pulay forces and stresses have to be corrected for during unit cell relaxations.

region. The situation can be remedied by introducing a so-called *pseudopotential* [77], which makes use of the fact that it is typically only the valence electrons, and not the core electrons, that participate in the chemical bonding. Accordingly, the pseudopotential is modified to achieve smoother variations of the wavefunction within the core region while still reproducing the correct all-electron wave function outside. This results in a dramatic decrease in the plane wave cutoff E_{cut} required for convergence and makes plane wave expansions feasible for practical calculations. The trade-off is one of introducing additional complexity; pseudopotentials need to be explicitly constructed for all atomic species involved and the size of the core region needs to be chosen appropriately. Pseudopotentials come in one of two different flavors: *norm-conserving* or *ultrasoft*, where the latter require lower cutoff energies. Ultrasoft pseudopotential have furthermore been shown to emerge naturally from the more rigorous framework of *projector augmented waves* (PAW) [97, 98]. Here, a linear transformation for converting between a valence and all-electron description is defined and different levels of treatment with regards to the core electrons are possible. For most practical purposes the initial core electron configuration for which the PAW potential was generated is kept throughout the calculation in what is called the *frozen core* approximation [99].

Another problem that emerges in periodic DFT calculations is that many properties, such as the total energy of the system, are given in terms of integrals over the first Brillouin zone (BZ) of the system

$$I = \frac{\Omega}{(2\pi)^3} \sum_{n}^{\text{occ}} \int_{\text{BZ}} d\boldsymbol{k}\, I_n(\boldsymbol{k}), \tag{4.32}$$

where I denotes some property, Ω the unit cell volume and the summation runs over all occupied bands. To numerically evaluate the $\boldsymbol{k}$-space integral, it is replaced by a summation over a finite amount of $\boldsymbol{k}$-points sampled from the Brillouin zone. A common sampling method is the Monkhorst-Pack scheme [100] where $M_1 \times M_2 \times M_3$ $\boldsymbol{k}$-points lie on an equidistant grid aligned with the reciprocal lattice vectors $\boldsymbol{b}_i$ according to the rule

$$\boldsymbol{k} = x_1\boldsymbol{b}_1 + x_2\boldsymbol{b}_2 + x_3\boldsymbol{b}_3 \quad \text{with} \quad x_i = \frac{2m_i - M_i - 1}{2M_i},\ m_i \in \{1, 2, \dots, M_i\}. \tag{4.33}$$

Furthermore, by properly weighting the terms in the summation approximating the integral Eq. (4.32), only those BZ $\boldsymbol{k}$-points that are inequivalent under the symmetries of the space group need to be included[2].

[2]The set of all such point is referred to as the irreducible Brillouin zone.

5

Summary of appended papers

5.1 Paper I

This paper originated as a means of gauging the accuracy of vdW-DF-cx (Sect. 4.1.4) in describing the prototypical chemisorption of molecules with long alkyl chains on a noble metal surface. In this context, earlier functionals in the vdW-DF family such as vdW-DF1 were underperforming due to gross overestimation of lattice constants, especially for the late transition metals Ag and Au. As a candidate system for the investigations, alkanethiolates on Au{111} were deemed particularly interesting, due to earlier work having failed to reproduce experimentally observed, vdW-related effects such as lying-down phases. The topic of thiolated monolayers on crystalline surfaces furthermore constitutes a technologically relevant system in its own right. The idea was thus to study the role of dispersive interaction in transitions between the experimentally observed low coverage lying-down phases and more dense standing up phases of the system using an ab initio thermodynamics model (Sect. 3.2).

The vdW-DF-cx functional was found to provide an excellent description, not only for the dispersive interactions but also the gold surface. Indeed, vdW-DF-cx offers significant improvement over the PBE values for both lattice constant and clean surface energy. Furthermore, lying-down phases, characterized by chemisorbed thiolates that lie almost parallel to the surface were revealed to be thermodynamically stable for alkyl chains with two or more methylene units. With increasing gas-phase chemical potential a transition to a standing-up phase was observed (Fig. 5.1). The most significant finding was that these transitions emerge due to a competition between alkyl chain-chain and chain-surface interactions. More precisely, the chain-surface interactions vary more steeply with the chain length, and the calculated interaction strength was shown to be in very good agreement with experimental data.

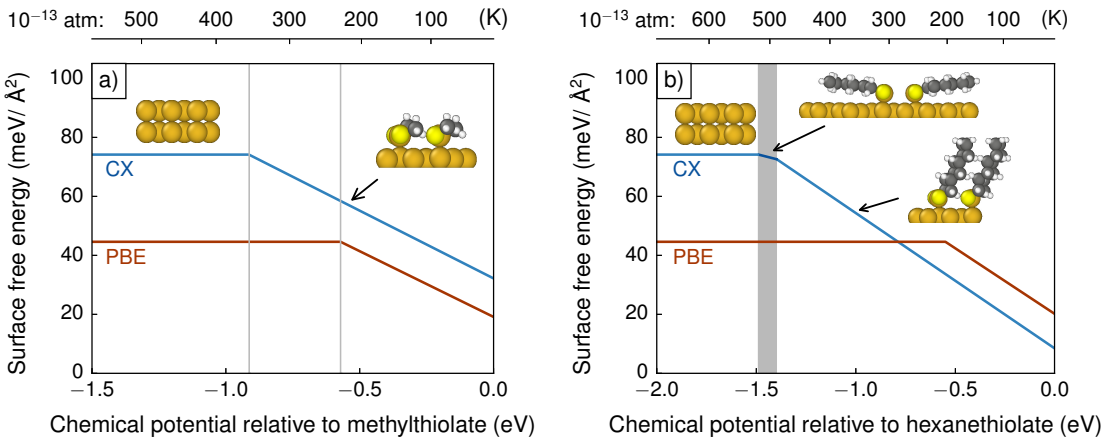

Figure 5.1: Phase stability curves for adsorption of gas-phase alkanethiolates on gold as a function of either the relative chemical potential of the adsorbates or, assuming ultra high vacuum conditions, the temperature. a) For methylthiolates only the clean surface and a dense monolayer are stable. b) For hexanethiolates an intermediate phase is also found where the alkyl chains are almost perpendicular to the surface due to dispersive interactions.

5.2 Paper II

Synthesis of colloidal NPs typically occurs in a rich chemical environment where the complex interplay between dissolved salts and surfactants with the NP surface is integral to determining the outcome. Whereas surfactants with long alkyl chains were the subject of study in **Paper I**, small adsorbates in the form of halide ions are the subject of the present paper.

As commonly occurring counterions in metal salts and crystalline phases of charged surfactants, such as CTAB, halides are almost always present in colloidal NP synthesis to some extent. In particular, Br^- and I^- are known to bind to metal surfaces in aqueous solution under ambient conditions and experimental evidence amassed over the years indicates that they often play a crucial role in determining the outcome of the synthesis. Accurate theoretical description of halide adsorption on metal surfaces under experimentally relevant conditions is thus of paramount importance if rational design of wet-chemical synthesis protocols is to be achieved. To this end, we address some of the technical as well as conceptual challenges that one is faced with in the DFT description of halide adsorption on Au and Pd surfaces. The major hurdle in this endeavor revolves around the treatment of solvation effects since explicitly including water molecules in a DFT calculation is computationally very expensive. We describe a thermodynamic model where DFT calculations are combined with experimental data

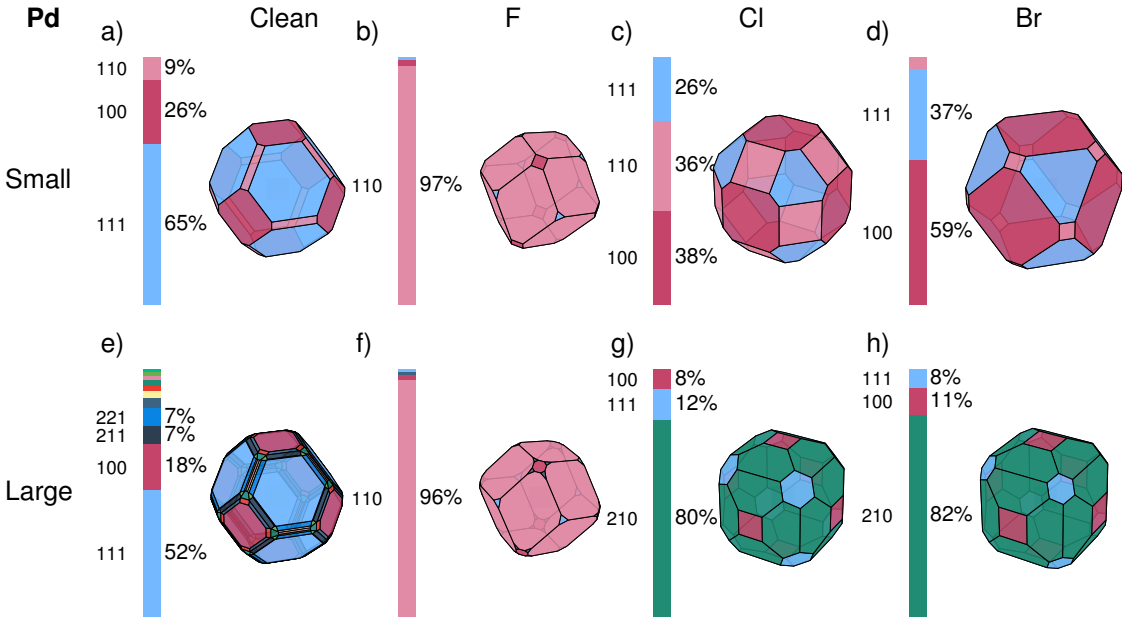

Figure 5.2: Wulff shapes for halide adsorption on Pd NPs under typical synthesis conditions of 0.1 M adsorbate concentration and ambient temperature and pressure. In a-d) results are shown for the small particle limit where only low-index facets are exposed by the NPs, while in the large particle limit e)-h) high-index facets are included. As we progress down the halogen group where {100} is stabilized at the expense of more open facets for small particles. The effect is not large enough, however, to change the stable shape to a nanocube. Note that I^- is left here due to convergence issues with the implicit solvation model.

to obtain a correct reference state for the solvated halide ions and explore the use of an implicit solvation model to incorporate surface-solvent interactions. Equipped with this model we show that equilibrium NP shapes can be be predicted as a function of the halide concentration [1]. The shape prediction is based on generalized Wulff constructions, which extend the regular Wulff construction to also include twinned particles.

From a more technical perspective, the importance of incorporating dispersive interactions at the DFT level is also highlighted. For instance, it is shown that they bring surface energies closer to experimental data and that qualitative as well as quantitative differences compared to conventional GGA-based functionals can be observed in the energetic ordering of different facets. It is furthermore established that surface-solvent interactions can significantly alter surface energies in a non-predictable fashion. Put

[1]Experimentally, this is the principal control parameter, yet the dependence of the adsorption energy on the concentration is often neglected in DFT studies.

together, these observations illustrate limitations in the transferability of results garnered from, e.g., PBE-based DFT studies of adsorption in vacuum to solvated systems.

5.3 Paper III

As demonstrated in **Paper II**, shape prediction for isotropic nanoparticles that are thermodynamic products can be satisfactorily modeled using first-principles methods. The growth of anisotropic nanoparticles, on the other hand, is typically heavily influenced by kinetics and prediction of the synthesis product requires a detailed knowledge of the reaction pathway. This is very much the case for the growth of gold nanorods, and in this paper we present a critical review of the current state of nanorod modeling and understanding of their growth mechanism. Due to the length and time scales involved, one must go beyond DFT to reach relevant system sizes, and the last few years have seen several investigations published based on MD simulations. Through these simulation, new light has been shed on the micellar structure assumed by CTAB on the surface of the nascent rods, which could potentially hold the key to understanding the growth. A large portion of our review is thus devoted to a discussion of these results and their implications, both in the light of experimental data and MD simulations carried out within our own group.

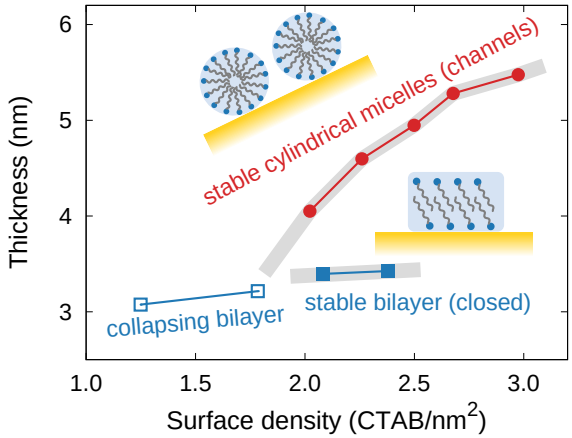

Figure 5.3: Quatitative landscape of micellar structures of CTAB on gold obtainable in MD simulations by varying the CTAB surface concentration and interdigination of the initial bilayer configuration. In additon to cyldrical micilles, bilayers and hemispherically-capped monolayers exist, illustrating the importance of the surface concentration and constraints imposed by kinetics. Growth models where a particular phase is assumed to prevail *a priori* should thus be met with caution.

A key discussion point is the surface phase diagram of CTAB on gold as a function of

concentration, as recent claims hold that CTAB forms cylindrical micelles on the surface rather than bilayers as has often been assumed. The presence of cylindrical micelles on a surface opens up for the possibility of monomers reaching the underlying surface by diffusing through channels located between neighboring cylinders. The existence of a facet-dependent anisotropy in one or more of the properties of the cylindrical micelles could then explain the subsequent anisotropy in the growth from a spherical particle to a rod. Indeed, the width of the channel openings has been proposed as such a property, but we argue that no systematic trend can be established when the CTAB concentration is varied. In fact, variation of the concentration leads to a landscape of micellar structures that, in addition to cylinders, features bilayers, spherical micelles and monolayers capped by hemispheres. We then proceed to discuss how anisotropic growth could arise given this more nuanced micellar landscape, including the possibility of a facet-dependence in the transition from a bilayer to a cylindrical shape.

5.4 Paper IV

An important aspect of modeling colloidal NPs concerns interparticle interactions, which are largely determined by what happens at the particle surface yet cannot be treated at the DFT level due to the upward shift in length and time scales. From an applications point of view, the ability to accurately describe the forces, both between NPs and between NP and the surfaces of a surrounding device, is important because it holds the key to rational system design. This work presents a joint theoretical and experimental contribution in this area, where a modeling framework based on DLVO theory is introduced for the purpose of systematically improving colloidal deposition setups. The main focus is on systems where depositing NPs need to be guided towards certain parts of a device. This is relevant, e.g., in the field of molecular electronics where guided deposition of particles interlinked by molecules enables parallel assembly of molecular circuits. To provide a common basis for the theoretical and experimental work, we consider a model system where citrate-stabilized AuNPs are guided towards pre-patterned, nanosized features (nanofeatures) on a SiO_2 substrate.

The first part of the paper concerns the selection of optimal materials. It is found that AuNPs can be preferentially directed towards Ni-covered features on a surface. This is rationalized in terms of the high Hamaker constant for Ni and the fact that Ni surfaces are positively charged under the experimental conditions. As a result, the electrostatic double layer interaction with the negatively charged AuNPs is attractive. The opposite behavior is observed for the clean SiO_2 substrate and hence deposition will only occur on the Ni-coated parts of the sample. Within our modeling framework, the choice of material for the nanofeatures can be be quantified in terms of the surface *deposition potential*, representing the lower potential threshold for which particle deposition is probable. The second part of the article deals with the geometry of the nanofea-

tures and its optimization for NP capture. We show that it is possible to systematically improve the chances of successfully capturing a nanoparticle, starting from a simple nanofeature design consisting of two parallel bars that are subsequently turned into forklift-shaped structures (Fig. 5.4). Optimal choices for the design parameters of the features can be predicted within our framework and the results agree reasonably well with experimental data.

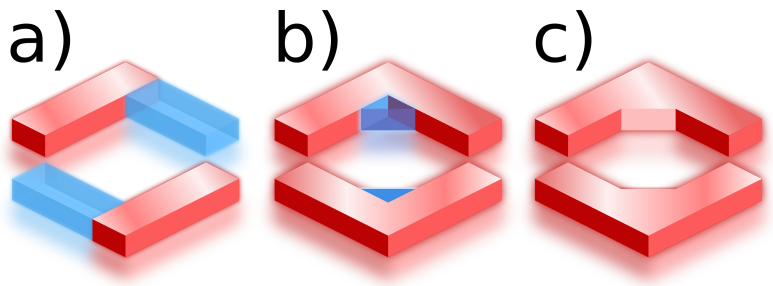

Figure 5.4: Successive improvements of a nanosized feature designed to capture nanoparticles. Starting from two parallel bars a) the sides can be extended to form a forklift-shaped structure b). In the final step the corners are cut away c), allowing a depositing to achieve greater proximity to the attractive nanofeature surfaces. Optimal choices of the design parameters can be determined using the our proposed framework based on DLVO theory.

In terms of the DLVO-based analysis, our framework work avoids two approximations that are commonly found in theoretical studies of deposition, namely the linearization of the Poisson-Boltzmann equation and the Derjaguin approximation. Instead, a computationally efficient approach to evaluating the electrostatic double layer interactions from numerical solutions to the non-linear Poisson-Boltzmann equation is presented. This allows us to take into account the asymmetric nature of the citrate electrolyte as well as surface potentials that extend beyond the linear regime. Departure from the Derjaguin approximation in favor of the surface element integration method allows us to represent interactions between surfaces also when their separation becomes comparable to the Debye length. The computational methodology is furthermore made available in terms of an extensible code written in `Python`.

5.5 Paper V

Dispersive interactions play a prominent role in this thesis. In particular for surface systems it has been argued (**Paper I**, **Paper II**) that incorporating non-local interactions is important for obtaining accurate results with DFT calculations. Here, a rigorous approach is provided by the vdW-DF framework and its associated functionals, which

have not been widely available since the non-trivial implementation has had to be repeated for each individual DFT code. In this work we seek to remedy this situation via the introduction of `libvdwxc`, a `C`-library that provides DFT codes with easy and efficient access to all vdW-DF family functionals. More precisely, the library computes the non-local vdW-DF correlation energy (Eq. (4.22)) given the density and its gradient as input from the interfacing DFT code. To obtain a specific vdW-DF functional, the non-local correlation energy thus obtained must be combined with the exchange part of the corresponding companion GGA functional and LDA correlation.

Due to the six-dimensional nature of the non-local correlation integral (Eq. (4.22)), direct integration is not viable. Instead, `libvdwxc` employs the method of Román-Pérez and Soler [89]. Briefly, the kernel is represented in terms of radial functions on a two-dimensional grid and spline-based interpolations are used to obtain high accuracy. The non-local correlation can then be computed using the convolution theorem, which reduces the six-dimensional integration to a summation over three-dimensional integrals. Several Fourier transforms must be calculated during this process, which limits the overall scaling of the method to $\mathcal{O}(n \log n)$ where n is the number of real-space grid points used.

The accuracy of the library is benchmarked over the S22 set of dimers[2] and good agreement with corresponding implementations in `VASP` and `Quantum Espresso` is obtained. Furthermore, parallelization is available through MPI; the scaling of parallel calculations with respect to the number of cores is measured for a ligand-protected AuNP consisting of 2424 atoms. It is found that the evaluation of the non-local correlation energy is generally efficient enough to not impose any additional limitations on system size compared to DFT calculations with conventional semi-local functionals.

[2]The data set consists of 22 dimers that generally exhibit dispersion and/or hydrogen bonding, with reference energies from accurate quantum chemical calculations.

A

Origin of the dispersive interaction

Each half of the cosmic breath, moved by a void.

Vektor, *Terminal Redux: Recharging the Void*

The origin of dispersive interactions and their asymptotic $1/R^6$-dependence can be demonstrated from elementary quantum mechanics, without appealing to classical concepts or a model system, by considering the interaction between two well-separated hydrogen atoms. A coordinate system according to Fig. A.1 is defined, where the nuclei a, b have a relative displacement $\boldsymbol{R}$ and the electrons are displaced from their respective parent nucleus by $\boldsymbol{r}_1$ and $\boldsymbol{r}_2$. The full non-relativistic, electronic Hamiltonian can be expressed as the sum of the Hamiltonians of each isolated atom plus an interaction term

$$H = \underbrace{-\frac{1}{2}\boldsymbol{p}_1^2 - \frac{1}{r_1}}_{\equiv H_a} \underbrace{-\frac{1}{2}\boldsymbol{p}_2^2 - \frac{1}{r_2}}_{\equiv H_b} + \underbrace{\left(\frac{1}{R} + \frac{1}{r_{12}} - \frac{1}{r_{1b}} - \frac{1}{r_{2a}}\right)}_{\equiv V}. \tag{A.1}$$

The idea is now to treat V as a perturbation on the Hamiltonian $H_0 = H_a + H_b$. Using the familiar labels (n, l, m) for the hydrogen atom quantum numbers, the energy eigenstates of the unperturbed Hamiltonian have the form

$$|p^{(0)}\rangle = |nlm\rangle_a \otimes |n'l'm'\rangle_b \equiv |nlm\rangle\,|n'l'm'\rangle\,, \tag{A.2}$$

where $p = (n, l, m, n', l', m')$ is a compound index and the (0) superscript indicates that the kets are only exact eigenstates for H_0 and not the full interacting Hamiltonian. The corresponding eigenvalues are

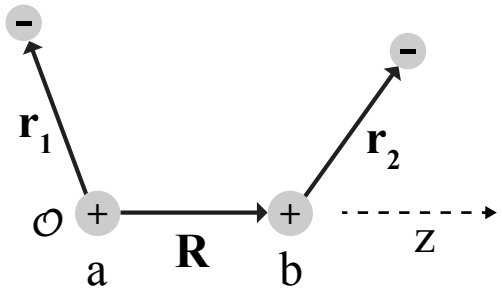

Figure A.1: Coordinate system used in the derivation of the dispersive interaction between two hydrogen atoms. The origin is taken to coincide with nucleus a and the z-axis is parallel to the relative displacement vector of the nuclei. Note that the displacement vector for the second electron is given relative to the parent nucleus rather than the origin.

$$\left\langle p^{(0)} \middle| H_0 \middle| p^{(0)} \right\rangle = \langle nlm \,|\, H_a \,|\, nlm \rangle + \langle n'l'm' \,|\, H_b \,|\, n'l'm' \rangle \equiv E^{(0)}_{n,n'} \tag{A.3}$$

and in particular the ground state energy is given by $E^{(0)}_{11} = -1\,\mathrm{Ha}$[1]. The next step is to write a multipole expansion of the perturbing potential by summing Taylor expansions of the individual terms in V. For the interaction of the first nuclei and the second electron:

$$\frac{1}{r_{2a}} = \frac{1}{|\boldsymbol{R} + \boldsymbol{r}_2|} = \frac{1}{R} + \frac{\boldsymbol{R} \cdot \boldsymbol{r}_2}{R^3} + \text{higher order terms.} \tag{A.4}$$

The other terms have similar expansions and upon summation of the results it is apparent that the monopole terms cancel as expected for neutral atoms. Furthermore, assuming that the atoms are well separated, i.e., $R >> a_0$ where a_0 is the Bohr radius, only the dipole term in Eq. (A.4) needs to be retained. The final expression is, after some algebra,

$$V \approx \frac{1}{R^3} \left(x_1 x_2 + y_1 y_2 - 2 z_1 z_2 \right). \tag{A.5}$$

The first order perturbation of the ground state energy is now evaluated as

$$W_1 = \frac{1}{R^3} \langle 100 \,|\, x_1 x_2 + y_1 y_2 - 2 z_1 z_2 \,|\, 100 \rangle = 0 \tag{A.6}$$

due to parity since $|100\rangle$ is even and V is odd. The second order perturbation cannot be exactly evaluated but is given by the series

[1] 1 Hartree (Ha) is equal to 2 Ry = 27.21138602(17) eV

$$W_2 = \sum_{n',n\neq 1} \sum_{\substack{l',m' \\ l,m}} \frac{\left|\langle 100|\,\langle 100\,|\,V\,|\,nlm\rangle\,|n'l'm'\rangle\right|^2}{E_{11}^{(0)} - E_{nn'}^{(0)}}, \tag{A.7}$$

where it is apparent that each term is negative and scales like $1/R^6$. It follows that to leading order the ground state energy of two well-separated neutral atoms can be written

$$E_0 = E_{11}^{(0)} + W_2 = -1 - \frac{C_6}{R^6}, \tag{A.8}$$

where C_6 is an unknown coefficient that needs to be calculated numerically. In conclusion, the correction W_2 describes a dipole-dipole type interaction, stemming from the electrostatic coupling the atoms experience in each others proximity. This is customarily referred to as the van der Waals interaction and results in a negative shift of the ground state energy. Since neither atom has a net dipole moment, the van der Walls interaction can be thought of as an induced dipole-induced dipole interaction as typically presented in literature. This simplified picture can, however, be misleading since it gives an impression that the phenomenon is time-dependent, when the above derivation shows that this is clearly not the case.

Acknowledgments

I wish to extend my most sincere thanks to my supervisor Paul Erhart for educating me in physics, references to popular culture, and so many other things. Above all else, however, I would like to thank you for teaching me the value of being perpetually curious. I am also grateful to my examiner Göran Wahnström for his wisdom, guidance and in particular for creating an open, inquisitive, and friendly working environment. It would of course not be much of a working environment without a set of wonderful colleagues; thank you all for your friendship, good conversation, and evenings at Foxes.

One of the greatest joys of working in a university is the proximity to virtually endless sources of inspiration and different perspectives. In this spirit I thank my co-supervisor Kasper Moth-Poulsen and all my collaborators, past, present (and future): Mikael Kuisma, Babak Sadigh, Christine Orme, Johnas Eklöf, Ask-Hjort Larsen, Henrik Grönbeck, Per Hyldgaard, Milica Todorovic and Patrick Rinke.

Last but not least, I extend my love and thanks to my family, girlfriend Emelie and close friends in Göteborg and all around the world. You brighten my days and keep me sane amidst all the equations.

Hoping to meet you again down the road,
Joakim

Bibliography

[1] A. H. Larsen, M. Kuisma, J. Löfgren, Y. Pouillon, P. Erhart, and P. Hyldgaard, "Libvdwxc: a library for exchange–correlation functionals in the vdW-DF family", Modelling and Simulation in Materials Science and Engineering **25**, 065004 (2017).

[2] L. B. Hunt, "The true story of purple of cassius", Gold Bulletin **9**, 134–139 (1976).

[3] D. Akinwande, N. Petrone, and J. Hone, "Two-dimensional flexible nanoelectronics", Nature Communications **5**, ncomms6678 (2014).

[4] Homberger Melanie and Simon Ulrich, "On the application potential of gold nanoparticles in nanoelectronics and biomedicine", Philosophical Transactions of the Royal Society A: Mathematical, Physical and Engineering Sciences **368**, 1405–1453 (2010).

[5] M. Su, F. Li, S. Chen, Z. Huang, M. Qin, W. Li, X. Zhang, and Y. Song, "Nanoparticle based curve arrays for multirecognition flexible electronics", Advanced Materials **28**, 1369–1374 (2016).

[6] A. H. Atabaki, S. Moazeni, F. Pavanello, H. Gevorgyan, J. Notaros, L. Alloatti, M. T. Wade, C. Sun, S. A. Kruger, H. Meng, K. A. Qubaisi, I. Wang, B. Zhang, A. Khilo, C. V. Baiocco, M. A. Popović, V. M. Stojanović, and R. J. Ram, "Integrating photonics with silicon nanoelectronics for the next generation of systems on a chip", Nature **556**, 349–354 (2018).

[7] S. K. Murthy, "Nanoparticles in modern medicine: state of the art and future challenges", Int J Nanomedicine **2**, 129–141 (2007).

[8] S. Tran, P.-J. DeGiovanni, B. Piel, and P. Rai, "Cancer nanomedicine: a review of recent success in drug delivery", Clinical and Translational Medicine **6**, 44 (2017).

[9] A. Dumas and P. Couvreur, "Palladium: a future key player in the nanomedical field?", Chemical Science **6**, 2153–2157 (2015).

[10] E. Serrano, G. Rus, and J. García-Martínez, "Nanotechnology for sustainable energy", Renewable and Sustainable Energy Reviews **13**, 2373–2384 (2009).

[11] S. F. Ahmed, M. Khalid, W. Rashmi, A. Chan, and K. Shahbaz, "Recent progress in solar thermal energy storage using nanomaterials", Renewable and Sustainable Energy Reviews **67**, 450–460 (2017).

[12] B. Bayatsarmadi, Y. Zheng, A. Vasileff, and S.-Z. Qiao, "Recent advances in atomic metal doping of carbon-based nanomaterials for energy conversion", Small **13**, 1700191 (2017).

[13] P. Zhang, A. Venkataraman, and C. Papadopoulos, "Self-assembled gold nanoparticle–molecular electronic networks", physica status solidi (b) **254**, 1700061 (2017).

[14] J. Eklöf-Österberg, T. Gschneidtner, B. Tebikachew, S. Lara-Avila, and K. Moth-Poulsen, "Parallel fabrication of self-assembled nanogaps for molecular electronic devices", Small **14**, 1803471 (2018).

[15] W. H. De Jong and P. J. Borm, "Drug delivery and nanoparticles: applications and hazards", International Journal of Nanomedicine **3**, 133–149 (2008).

[16] S. A. A. Rizvi and A. M. Saleh, "Applications of nanoparticle systems in drug delivery technology", Saudi Pharmaceutical Journal **26**, 64–70 (2018).

[17] B. Klębowski, J. Depciuch, M. Parlińska-Wojtan, and J. Baran, "Applications of noble metal-based nanoparticles in medicine", International Journal of Molecular Sciences **19** (2018) 10.3390/ijms19124031.

[18] B. Hammer and J. K. Nørskov, "Electronic factors determining the reactivity of metal surfaces", Surface Science **343**, 211–220 (1995).

[19] D. Astruc, "Transition-metal nanoparticles in catalysis: from historical background to the state-of-the art", in *Nanoparticles and catalysis* (John Wiley & Sons, Ltd, 2008), pp. 1–48.

[20] M. Rycenga, C. M. Cobley, J. Zeng, W. Li, C. H. Moran, Q. Zhang, D. Qin, and Y. Xia, "Controlling the synthesis and assembly of silver nanostructures for plasmonic applications", Chemical Reviews **111**, 3669–3712 (2011).

[21] R. J. Warmack and S. L. Humphrey, "Observation of two surface-plasmon modes on gold particles", Physical Review B **34**, 2246–2252 (1986).

[22] X. Huang, I. H. El-Sayed, W. Qian, and M. A. El-Sayed, "Cancer cell imaging and photothermal therapy in the near-infrared region by using gold nanorods", Journal of the American Chemical Society **128**, 2115–2120 (2006).

[23] L. Wang, Y. Liu, W. Li, X. Jiang, Y. Ji, X. Wu, L. Xu, Y. Qiu, K. Zhao, T. Wei, Y. Li, Y. Zhao, and C. Chen, "Selective targeting of gold nanorods at the mitochondria of cancer cells: implications for cancer therapy", Nano Letters **11**, 772–780 (2011).

[24] C. Wadell, S. Syrenova, and C. Langhammer, "Plasmonic hydrogen sensing with nanostructured metal hydrides", ACS Nano **8**, 11925–11940 (2014).

[25] M. Semmler, J. Seitz, F. Erbe, P. Mayer, J. Heyder, G. Oberdörster, and W. G. Kreyling, "Long-term clearance kinetics of inhaled ultrafine insoluble iridium particles from the rat lung, including transient translocation into secondary organs", Inhalation Toxicology **16**, 453–459 (2004).

[26] J. F. Hillyer and R. M. Albrecht, "Gastrointestinal persorption and tissue distribution of differently sized colloidal gold nanoparticles", Journal of Pharmaceutical Sciences **90**, 1927–1936 (2001).

[27] M. Longmire, P. L. Choyke, and H. Kobayashi, "Clearance properties of nanosized particles and molecules as imaging agents: considerations and caveats", Nanomedicine (Lond) **3**, 703–717 (2008).

[28] K.-T. Rim, S.-W. Song, and H.-Y. Kim, "Oxidative DNA damage from nanoparticle exposure and its application to workers' health: a literature review", Saf Health Work **4**, 177–186 (2013).

[29] M. Faraday, "The bakerian lecture: experimental relations of gold (and other metals) to light", Phil. Trans. R. Soc. Lond. **147**, 145–181 (1857).

[30] M. C. Lea, "On allotropic forms of silver", American Journal of Science **Series 3 Vol. 38**, 47–49 (1889).

[31] B. Jirgersons and M. E. Straumanis, "Chapter 12 - tthe preparation of colloidal solutions", in *A short textbook of colloid chemistry (second revised edition)* (Pergamon, 1962), pp. 293–322.

[32] A. Einstein, "On the movement of small particles suspended in stationary liquids required by the molecular-kinetic theory of heat", Annalen der Physik **17**, 549–560 (1905).

[33] M. Smoluchowski, "Zur kinetischen theorie der brown'schen molekularbewegung und der suspensionen", Annalen der Physik **21**, 756–781 (1906).

[34] G. Mie, "Beiträge zur optik trüber medien, speziell kolloidaler metallösungen", Annalen der Physik **330**, 377–445 (1908).

[35] R. Gans, "Über die form ultramikroskopischer goldteilchen", Annalen der Physik **342**, 881–900 (1912).

[36] N. Kumar and S. Kumbhat, *Essentials in nanoscience and nanotechnology* (John Wiley & Sons, Apr. 11, 2016), 506 pp.

[37] Y. Huttel, *Gas-phase synthesis of nanoparticles* (John Wiley & Sons, June 19, 2017), 416 pp.

[38] B. L. Cushing, V. L. Kolesnichenko, and C. J. O'Connor, "Recent advances in the liquid-phase syntheses of inorganic nanoparticles", Chemical Reviews **104**, 3893–3946 (2004).

[39] J. Turkevich, P. Cooper Stevenson, and J. Hillier, "A study of the nucleation and growth processes in the synthesis of colloidal gold", Discussions of the Faraday Society **11**, 55–75 (1951).

[40] N. R. Jana, L. Gearheart, and C. J. Murphy, "Wet chemical synthesis of high aspect ratio cylindrical gold nanorods", Journal of Physical Chemistry B **105**, 4065–4067 (2001).

[41] N. R. Jana, L. Gearheart, and C. J. Murphy, "Evidence for seed-mediated nucleation in the chemical reduction of gold salts to gold nanoparticles", Chemistry of Materials **13**, 2313–2322 (2001).

[42] J. Zeng, C. Zhu, J. Tao, M. Jin, H. Zhang, Z.-Y. Li, Y. Zhu, and Y. Xia, "Controlling the nucleation and growth of silver on palladium nanocubes by manipulating the reaction kinetics", Angewandte Chemie International Edition **51**, 2354–2358 (2012).

[43] C. M. Liu, L. Guo, H. B. Xu, Z. Y. Wu, and J. Weber, "Seed-mediated growth and properties of copper nanoparticles, nanoparticle 1d arrays and nanorods", Microelectronic Engineering, Proceedings of the 8th International Conference on Electronic Materials (IUMRS-ICEM2002) **66**, 107–114 (2003).

[44] G. W. Sławiński and F. P. Zamborini, "Synthesis and alignment of silver nanorods and nanowires and the formation of pt, pd, and core/shell structures by galvanic exchange directly on surfaces", Langmuir **23**, 10357–10365 (2007).

[45] D. Seo, C. I. Yoo, J. Jung, and H. Song, "Ag-au-ag heterometallic nanorods formed through directed anisotropic growth", Journal of the American Chemical Society **130**, 2940–2941 (2008).

[46] C. Gao, J. Goebl, and Y. Yin, "Seeded growth route to noble metal nanostructures", Journal of Materials Chemistry C **1**, 3898–3909 (2013).

[47] B. Nikoobakht and M. A. El-Sayed, "Preparation and growth mechanism of gold nanorods (NRs) using seed-mediated growth method", Chemistry of Materials **15**, 1957–1962 (2003).

[48] S. Javadian, V. Ruhi, A. Heydari, A. Asadzadeh Shahir, A. Yousefi, and J. Akbari, "Self-assembled CTAB nanostructures in aqueous/ionic liquid systems: effects of hydrogen bonding", Industrial and Engineering Chemistry Research **52**, 4517–4526 (2013).

[49] C. J. Johnson, E. Dujardin, S. A. Davis, C. J. Murphy, and S. Mann, "Growth and form of gold nanorods prepared by seed-mediated, surfactant-directed synthesis", Journal of Materials Chemistry **12**, 1765–1770 (2002).

[50] S. E. Lohse and C. J. Murphy, "The quest for shape control: a history of gold nanorod synthesis", Chemistry of Materials **25**, 1250–1261 (2013).

[51] E. Carbó-Argibay, B. Rodríguez-González, S. Gómez-Graña, A. Guerrero-Martínez, I. Pastoriza-Santos, J. Pérez-Juste, and L. M. Liz-Marzán, "The crystalline structure of gold nanorods revisited: evidence for higher-index lateral facets", Angewandte Chemie International Edition **49**, 9397–9400 (2010).

[52] B. Goris, S. Bals, W. Van den Broek, E. Carbó-Argibay, S. Gómez-Graña, L. M. Liz-Marzán, and G. Van Tendeloo, "Atomic-scale determination of surface facets in gold nanorods", Nature Materials **11**, 930–935 (2012).

[53] X. Ye, C. Zheng, J. Chen, Y. Gao, and C. B. Murray, "Using binary surfactant mixtures to simultaneously improve the dimensional tunability and monodispersity in the seeded growth of gold nanorods", Nano Letters **13**, 765–771 (2013).

[54] S. Koeppl, C. Solenthaler, W. Caseri, and R. Spolenak, "Towards a reproducible synthesis of high aspect ratio gold nanorods", Journal of Nanomaterials **2011**, 1–13 (2011).

[55] C. F. Bohren and D. R. Huffman, "Particles small compared with the wavelength", in *Absorption and scattering of light by small particles* (Wiley-VCH Verlag GmbH, 1998), pp. 130–157.

[56] A. S. Barnard, "Modelling of nanoparticles: approaches to morphology and evolution", Reports on Progress in Physics **73**, 086502 (2010).

[57] G. Wulff, "Zur frage der geschwindigkeit des wachstums und der auflösung der krystallflagen", Zeitschrift für Krystallographie und Mineralogie **34**, 449–530 (1901).

[58] R. F. S.-. Constable, *Kinetics and mechanism of crystallization* (Elsevier Science & Technology Books, 1968).

[59] C. J. Cramer, *Essentials of computational chemistry: theories and models* (Wiley, June 24, 2005), 620 pp.

[60] J. Rogal, K. Reuter, and M.-P.-G. z. F. d. W. Fritz-Haber-Institut, *Ab initio atomistic thermodynamics for surfaces: a primer*, AD-a476 575 (Defense Technical Information Center, 2006).

[61] K. A. Persson, B. Waldwick, P. Lazic, and G. Ceder, "Prediction of solid-aqueous equilibria: scheme to combine first-principles calculations of solids with experimental aqueous states", Physical Review B **85**, 235438 (2012).

[62] P. Hunenberger and M. Reif, *Single-ion solvation* (Apr. 18, 2011).

[63] H. Sellers, E. M. Patrito, and P. P. Olivera, "Thermodynamic and ab initio calculations of chemisorption energies of ions", Surface Science **356**, 222–232 (1996).

[64] K. Mathew, R. Sundararaman, K. Letchworth-Weaver, T. A. Arias, and R. G. Hennig, "Implicit solvation model for density-functional study of nanocrystal surfaces and reaction pathways", The Journal of Chemical Physics **140**, 084106 (2014).

[65] K. Mathew and R. G. Hennig, "Implicit self-consistent description of electrolyte in plane-wave density-functional theory", arXiv:1601.03346 [cond-mat] (2016).

[66] V. Sharma, K. Park, and M. Srinivasarao, "Colloidal dispersion of gold nanorods: historical background, optical properties, seed-mediated synthesis, shape separation and self-assembly", Materials Science and Engineering: R: Reports **65**, 1–38 (2009).

[67] J. N. Israelachvili, *Intermolecular and surface forces* (Academic Press, May 29, 2015), 706 pp.

[68] H. C. Hamaker, "The london—van der waals attraction between spherical particles", Physica **4**, 1058–1072 (1937).

[69] M. R. Wright, *An introduction to aqueous electrolyte solutions* (John Wiley & Sons, June 5, 2007), 603 pp.

[70] R. Hogg, T. W. Healy, and D. W. Fuerstenau, "Mutual coagulation of colloidal dispersions", Transactions of the Faraday Society **62**, 1638–1651 (1966).

[71] L. R. White, "On the deryaguin approximation for the interaction of macrobodies", Journal of Colloid and Interface Science **95**, 286–288 (1983).

[72] S. Bhattacharjee and M. Elimelech, "Surface element integration: a novel technique for evaluation of DLVO interaction between a particle and a flat plate", Journal of Colloid and Interface Science **193**, 273–285 (1997).

[73] S. Bhattacharjee, M. Elimelech, and M. Borkovec, "DLVO interaction between colloidal particles: beyond derjaguin's approximation", Croatica Chemica Acta **71**, 883–903 (1998).

[74] M. Born and R. Oppenheimer, "Zur quantentheorie der molekeln", Annalen der Physik **389**, 457–484 (1927).

[75] P. Hohenberg and W. Kohn, "Inhomogeneous electron gas", Physical Review **136**, B864–B871 (1964).

[76] E. Engel and R. M. Dreizler, *Density functional theory*, Theoretical and Mathematical Physics (Springer, Berlin, Heidelberg, 2011).

[77] R. M. Martin, *Electronic structure: basic theory and practical methods*, 1st ed. (Cambridge University Press, 2004).

[78] W. Kohn and L. J. Sham, "Self-consistent equations including exchange and correlation effects", Physical Review **140**, A1133–A1138 (1965).

[79] J. P. Perdew, K. Burke, and M. Ernzerhof, "Generalized gradient approximation made simple", Physical Review Letters **77**, 3865–3868 (1996).

[80] S. Grimme, "Accurate description of van der waals complexes by density functional theory including empirical corrections", Journal of Computational Chemistry **25**, 1463–1473 (2004).

[81] J. Klimeš and A. Michaelides, "Perspective: advances and challenges in treating van der waals dispersion forces in density functional theory", The Journal of Chemical Physics **137**, 120901 (2012).

[82] S. Grimme, "Semiempirical GGA-type density functional constructed with a long-range dispersion correction", Journal of Computational Chemistry **27**, 1787–1799 (2006).

[83] S. Grimme, J. Antony, S. Ehrlich, and H. Krieg, "A consistent and accurate ab initio parametrization of density functional dispersion correction (DFT-d) for the 94 elements h-pu", The Journal of Chemical Physics **132**, 154104 (2010).

[84] A. D. Becke and E. R. Johnson, "A density-functional model of the dispersion interaction", The Journal of Chemical Physics **123**, 154101 (2005).

[85] A. Tkatchenko and M. Scheffler, "Accurate molecular van der waals interactions from ground-state electron density and free-atom reference data", Physical Review Letters **102**, 073005 (2009).

[86] Y. Zhao and D. G. Truhlar, "Density functionals for noncovalent interaction energies of biological importance", Journal of Chemical Theory and Computation **3**, 289–300 (2007).

[87] K. Berland, "Connected by voids: interactions and screening in sparse matter", Doctoral thesis (Chalmers University of Technology, 2012).

[88] K. Berland, V. R. Cooper, K. Lee, E. Schröder, T. Thonhauser, P. Hyldgaard, and B. I. Lundqvist, "Van der waals forces in density functional theory: a review of the vdW-DF method", Reports on Progress in Physics **78**, 066501 (2015).

[89] G. Román-Pérez and J. M. Soler, "Efficient implementation of a van der waals density functional: application to double-wall carbon nanotubes", Physical Review Letters **103**, 096102 (2009).

[90] M. Dion, H. Rydberg, E. Schröder, D. C. Langreth, and B. I. Lundqvist, "Van der waals density functional for general geometries", Physical Review Letters **92**, 246401 (2004).

[91] Kyuho Lee, Éamonn D. Murray, Lingzhu Kong, Bengt I. Lundqvist, and David C. Langreth, "Higher-accuracy van der waals density functional", Physical Review B **82** (2010) 10.1103/PhysRevB.82.081101.

[92] Y. Zhang and W. Yang, "Comment on "generalized gradient approximation made simple"", Physical Review Letters **80**, 890–890 (1998).

[93] É. D. Murray, K. Lee, and D. C. Langreth, "Investigation of exchange energy density functional accuracy for interacting molecules", Journal of Chemical Theory and Computation **5**, 2754–2762 (2009).

[94] K. Berland and P. Hyldgaard, "Exchange functional that tests the robustness of the plasmon description of the van der waals density functional", Physical Review B **89**, 035412 (2014).

[95] L. Gharaee, P. Erhart, and P. Hyldgaard, "Finite-temperature properties of nonmagnetic transition metals: comparison of the performance of constraint-based semilocal and nonlocal functionals", Physical Review B **95**, 085147 (2017).

[96] N. W. Ashcroft and N. D. Mermin, *Solid state physics* (Holt, Rinehart and Winston, 1976).

[97] P. E. Blöchl, "Projector augmented-wave method", Physical Review B **50**, 17953–17979 (1994).

[98] G. Kresse and D. Joubert, "From ultrasoft pseudopotentials to the projector augmented-wave method", Physical Review B **59**, 1758–1775 (1999).

[99] A. Kiejna, G. Kresse, J. Rogal, A. De Sarkar, K. Reuter, and M. Scheffler, "Comparison of the full-potential and frozen-core approximation approaches to density-functional calculations of surfaces", Physical Review B **73**, 035404 (2006).

[100] H. J. Monkhorst and J. D. Pack, "Special points for brillouin-zone integrations", Physical Review B **13**, 5188–5192 (1976).